

# Post-AGB candidate IRAS 02143+5852: Cepheid-like variability, three-layer circumstellar dust envelope and spectral features

N.P. Ikonnikova<sup>1\*</sup>, M.A. Burlak<sup>1</sup>, A.V. Dodin<sup>1</sup>, S.Yu. Shugarov<sup>1,2</sup>, A.A. Belinski<sup>1</sup>,  
A.A. Fedoteva<sup>1</sup>, A.M. Tatarnikov<sup>1,3</sup>, R.J. Rudy<sup>4</sup>, R.B. Perry<sup>5</sup>, S.G. Zheltoukhov<sup>1,3</sup>,  
K.E. Atapin<sup>1</sup>

<sup>1</sup>*Sternberg Astronomical Institute, Lomonosov Moscow State University, Moscow 119234, Russia*

<sup>2</sup>*Astronomical Institute of the Slovak Academy of Sciences, Tatranska Lomnica 05960, Slovakia*

<sup>3</sup>*Faculty of Physics, Lomonosov Moscow State University, Moscow 119991, Russia*

<sup>4</sup>*Kookoosint Scientific, 1530 Calle Portada, Camarillo, CA 93010, USA*

<sup>5</sup>*Alabaster Scientific, P.O. Box 120, Irvington, VA 22480, USA*

Accepted 2024. Received 2023; in original form 2023

## ABSTRACT

We present the results of multicolour  $UBVR_CI_CJHK$  photometry, spectroscopic analysis and spectral energy distribution (SED) modelling for the post-AGB candidate IRAS 02143+5852. We detected Cepheid-like light variations with the full peak-to-peak amplitude  $\Delta V \sim 0.9$  mag and the pulsation period of about 24.9 d. The phased light curves appeared typical for the W Vir Cepheids. The period-luminosity relation for the Type II Cepheids yielded the luminosity  $\log L/L_\odot \sim 2.95$ . From a low-resolution spectrum, obtained at maximum brightness, the following atmospheric parameters were determined:  $T_{\text{eff}} \sim 7400$  K and  $\log g \sim 1.38$ . This spectrum contains the emission lines  $H\alpha$ ,  $\text{Ba II } \lambda 6496.9$ ,  $\text{He I } \lambda 10830$  and  $\text{Pa}\beta$ . Spectral monitoring performed in 2019–2021 showed a significant change in the  $H\alpha$  profile and appearance of CH and CN molecular bands with pulsation phase. The metal lines are weak. Unlike typical W Vir variables, the star shows a strong excess of infrared radiation associated with the presence of a heavy dust envelope around the star. We modelled the SED using our photometry and archival data from different catalogues and determined the parameters of the circumstellar dust envelope. We conclude that IRAS 02143+5852 is a low-luminosity analogue of dusty RV Tau stars.

**Key words:** stars: AGB and post-AGB – stars: circumstellar matter – stars: variables: general: individual: IRAS 02143+5852 – stars.

## 1 INTRODUCTION

IRAS 02143+5852 ( $02^{\text{h}}17^{\text{m}}57^{\text{s}}.8, +59^{\circ}05'52''$ , 2000) is an infrared (IR) source mentioned for the first time by [Manchado et al. \(1989\)](#) as an object with the far-IR colours similar to those of planetary nebulae. These authors suggested that the object is in the post-AGB stage of evolution. From this point on, the star began to be studied together with other post-AGB candidates. [Omont et al. \(1993\)](#) considered it as a carbon-rich proto-planetary nebula (PPN). Observations in the near-IR were carried out by [García-Lario et al. \(1990\)](#), [Fujii et al. \(2002\)](#), [Ueta et al. \(2003\)](#) and [Cooper et al. \(2013\)](#). [Ueta et al. \(2003\)](#) pointed out that the  $H$  and  $K'$  magnitudes showed a slight variation compared to previous observations. Extended dust shells

have been found in a number of post-AGB stars, however IRAS 02143+5852 is unresolved at  $11\ \mu\text{m}$  ([Meixner et al. 1999](#)). [Gledhill \(2005\)](#) did not detect polarization within errors in the  $J$ -band. No  $\text{H}_2\text{O}$  maser emission was detected by [Suárez et al. \(2007\)](#).

[Fujii et al. \(2002\)](#) were the first to obtain optical magnitudes for the star:  $B = 14.96$  mag and  $V = 13.74$  mag. The authors assumed the star to be of F5Ib spectral type with corresponding temperature  $T_{\text{eff}} = 6900$  K, intrinsic colour  $(B-V)_0 = 0.33$  mag and colour excess  $E(B-V) = 0.89$  mag. [Fujii et al. \(2002\)](#) analysed the SED spanning the optical to far-IR wavelengths and obtained an estimate for the dust shell temperature  $T_{\text{dust}} = 205$  K.

The spectral type of the object is not clear. [Kelly & Hrivnak \(2005\)](#) classified the IRAS 02143+5852 spectrum as an Ae one. Based on a low-resolution spectrum, [Suárez et al. \(2006\)](#) stated an F7Ie spectral type.

\* E-mail: ikonnikova@sai.msu.ru

Analysing the spectrum presented in the appendix of the above paper, [Molina \(2018\)](#) found  $T_{\text{eff}} = 7967 \pm 91$  K. [Sivarani & Parthasarathy \(2004\)](#) noted that the optical spectrum showed strong Balmer lines in absorption and no helium lines.

The light variability of the star was discovered based on the All Sky Automated Survey for SuperNovae (ASAS-SN) data ([Shappee et al. 2014](#); [Kochanek et al. 2017](#)). In the ASAS-SN catalogue of variable stars ([Jayasinghe et al. 2019](#)), it has the designation ASASSN-V J021757.82+590552.0, a period of 50.18 d and an YSO (Young Stellar Object) variability type. The star is also contained in the ZTF catalogue of periodic variable stars ([Chen et al. 2020](#)), where it is designated as ZTFJ021757.80+590552.1, has period 25.1385074 d, and is classified as CepII (Cepheid variable).

In this paper, we present new photometric and spectroscopic observations of IRAS 02143+5852 obtained in 2017–2021. These data allowed us to detect light variability and to study its character, as well as to determine the parameters ( $T_{\text{eff}}$ ,  $\log g$ ) of the star and to investigate spectrum change. We have used all currently available IR photometric data to perform the SED modelling aiming to probe the properties of the circumstellar material.

The paper is organized as follows. Photometric and spectroscopic observations and data reduction procedures are described in Section 2. In Section 3 we analyse photometric data. Section 4 presents the results of low-resolution spectroscopy. In Section 5 we discuss the evolutionary status of the star. Section 6 is devoted to the SED modelling. In Section 7 we discuss the obtained results and the star’s similarity to known objects. Section 8 presents our conclusions.

## 2 OBSERVATIONS AND DATA REDUCTION

### 2.1 $UBVR_{CI}$ photometry

The photometric observations of IRAS 02143+5852 were carried out with the FLI ML3041 CCD (2048×2048 pixels, the pixel size 15  $\mu\text{m}$ ) mounted on the 0.6-m telescope of the Stará Lesná Observatory of the Astronomical Institute of Slovak Academy of Science (SI600) in 2018–2019 and with the Andor iKon-L BV camera (2048×2048 pixels, the pixel size 13.5  $\mu\text{m}$ ) mounted on the new 0.6-m telescope (RC600) installed at the Caucasian Mountain Observatory (CMO) of the Sternberg Astronomical Institute of the Moscow State University (for more details see [Berdnikov et al. \(2020\)](#)) in 2019–2021. Each detector was equipped with a set of Johnson-Cousins  $UBVR_{CI}$  filters. Standard data reduction procedures (de-biasing, flat-fielding, darkening) and aperture photometry were performed using the MAXIM DL5 package and self-developed PYTHON scripts. The mean photometric uncertainty is about 0.005–0.010 mag for the  $B$ ,  $V$ ,  $R_C$ ,  $I_C$  bands and up to 0.05 for the  $U$  band.

Information on the comparison stars, used for differential photometry, is presented in Table 1. The magnitudes for the comparison stars were acquired via referencing to photometric standards in the S23-246 and S23-436 fields ([Landolt 2013](#)). The  $R_C$  image of IRAS 02143+5852 and comparison stars is shown in Fig. 1. The  $UBVR_{CI}$ -photometry is presented in Table A1 where for every night we list the mean time of observation and magnitudes in each of photometric bands averaged over 2–3 frames.

**Table 1.** The comparison stars for  $UBVR_{CI}$  photometry.

Star	$U$	$B$	$V$	$R_C$	$I_C$
st1	14.841	13.932	12.629	11.840	11.052
st2	14.802	14.417	13.512	12.998	12.524

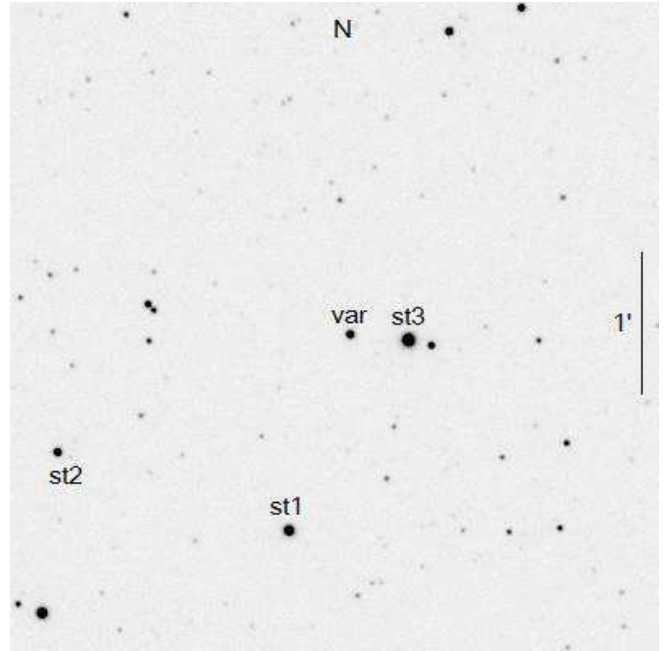


**Figure 1.** The  $R_C$ -band image of the IRAS 02143+5852 (var) field with the comparison stars marked. This CCD-frame was obtained with RC600 on February 15, 2020.

### 2.2 $JHK$ -photometry

The  $JHK$ -photometry was obtained from 2017 November 6 to 2021 February 18 (73 nights in total) with the ASTRONomical Near-InfraRed CAMera (ASTRONIRCAM) ([Nadjip et al. 2017](#)) mounted on the 2.5-m telescope of CMO. We used the dithering mode to obtain images in the  $JHK$  bands of the MKO–NIR system (Mauna Kea Observatories Near-InfraRed ([Simons and Tokunaga 2002](#))). Each frame was automatically reduced and calibrated using the pipeline described in detail in [Tatarnikov et al. \(2023\)](#). The standard reduction procedures were performed including the correction for non-linearity and bad pixels, dark subtraction, flat-fielding and background subtraction. The instrumental magnitudes for the star were derived using differential aperture-based photometry with respect to 2MASS stars (Fig. 1, Table 2) which magnitudes were converted to the MKO–NIR system following the equations from [Leggett et al. \(2006\)](#). The  $JHK$ -photometry in the MKO–NIR and 2MASS systems is presented in Table B1.

As we obtained several frames for each filter during each pointing, uncertainties were calculated as standard deviations. The average uncertainties are  $\Delta J = 0.011$  mag,  $\Delta H = 0.010$  mag,  $\Delta K = 0.012$  mag.

**Table 2.** The comparison stars for *JHK* photometry.

Star	<i>J</i> (2MASS)	<i>H</i> (2MASS)	<i>K</i> (2MASS)
St1	9.977	9.345	9.168
St3	9.977	9.776	9.705

**Table 3.** Spectroscopic observations of IRAS 02143+5852 on SAI CMO

N <sup>o</sup>	Date yyyy-mm-dd	HJD	Exposure time, s	Standard stars
1	2020-01-18	2458867.30	300×1	BD+25°4655
2	2020-01-20	2458869.28	300×1	BD+25°4655
3	2020-02-26	2458906.25	900×1	HR1544
4	2020-03-03	2458912.21	600×3	Hiltner 600
5	2020-08-30	2459093.51	600×1	BD+28°4211
6	2020-09-06	2459099.33	1200×1	BD+28°4211
7	2020-09-12	2459105.49	1200×1	HR153
8	2020-09-23	2459116.46	600×1	HR153
9	2020-11-01	2459155.34	600×3	BD+28°4211
10	2020-12-14	2459198.18	600×3	HR1544
11	2021-02-05	2459251.34	600×2	Feige 66
12	2021-02-11	2459257.20	600×2	HR718

### 2.3 Spectroscopy

A low-resolution optical and near-IR spectrum of IRAS 02143+5852 was obtained on the 3-m telescope of the Lick Observatory (USA) with the Aerospace Corporation’s Visible and Near Infrared Imaging Spectrograph (VNIRIS) (Rudy et al. 2021) (0.46–2.5  $\mu\text{m}$ ,  $R \sim 700$ ) on 2018 October 20 (JD 2458412.5). The spectra were calibrated using the solar-type standard star HIP 9829.

Low-resolution spectra were acquired on the 2.5-m telescope of CMO via the Transient Double-beam Spectrograph (TDS) equipped with two Andor Newton 940P cameras using E2V CCD42-10 detectors, and volume phase holographic gratings (see Potanin et al. (2020)). A 1''0 slit was used. The log of observations is given in Table 3. The data reduction procedures including dark and flat-field correction, cosmic ray removal, two-dimensional wavelength linearization, background subtraction, and relative flux calibration using spectrophotometric standards listed in Table 3 were performed using PYTHON scripts.

## 3 PHOTOMETRIC ANALYSIS

In Fig. 2 we present the *UBVR<sub>C</sub>IC* light and colour curves for the period from 2019 August to 2020 March which was best covered by observations. A periodic variation is clearly seen both in light and colour curves. The shape of light curve differs from band to band being sawtooth in the *U* band while the *R<sub>C</sub>* and *I<sub>C</sub>* light rapidly rises to a flat and long-lasting maximum. There is a bump on the declining branch of the *B* and *V* light curves. One can also see that deeper minima alternate with shallower ones and this effect is most pronounced in the *U* and *B* bands and in the *B – V* colour. The *BVR<sub>C</sub>IC* light curves of IRAS 02143+5852 are very sim-

ilar to those of W Vir which is the Type II Cepheid prototype (Templeton & Henden 2007).

The near-IR light curves spanning the whole observational period are shown in Fig. 3. As can be seen, the *JHK*-brightness varies with a peak-to-peak amplitude of about 1 mag.

### 3.1 Periodicity analysis

In order to study the periodicities, we have used the WINEFK code developed by V.P. Goranskii<sup>1</sup>. This code implements the well-known method of minimizing the phase dispersion (Lafler & Kinman 1965) and the discrete Fourier transform for arbitrarily distributed time series (Deeming 1975).

The Fourier spectra of our *V*-band data presented in Table A1 is shown in Fig 4. In the frequency spectrum obtained by the Deeming method a peak corresponding to a period of 24.885 d is dominant (Fig. 4 (a)). There are two weaker peaks on both sides of the primary one which turn out its one-year aliases. Taking into consideration all our *UBVR<sub>C</sub>IC* data for the 2018–2021 interval we derived  $P = 24.885 \pm 0.150$  d.

Analysing the times of maxima allowed us to revise the ephemeris to be:

$$\text{JD}(\text{max}) = 2458660.352 + 24.885 \times E \quad (1)$$

where ‘maximum’ is defined as a peak at the end of the rising branch.

The Lafler-Kinman method gives a frequency spectrum that contains peaks corresponding to the period of 24.885 d, and its multiples of 49.736 and 74.635 d (Fig 4 (b)).

The light curves folded on the 24.885 d period show a significant scatter ( $>0.1$  mag) at phase 0.6–1.0 which is much larger than observation errors indicating that there are cycle-to-cycle variations. Folding on twice the above period reveals some details in light curves, particularly, the alteration of deep and shallow minima. The *UBVR<sub>C</sub>IC* light curves folded on periods of 24.885 and 49.736 d are shown in Fig. 5.

The near-IR data are less numerous than the optical data, so, it is harder to determine reliable period. The power spectrum derived by the Lafler-Kinman method for periods in the range 10–100 d is dominated by the peaks which correspond to the periods of 24.819 d and 49.690 d (*J*-band), 24.793 d and 49.690 d (*H* and *K* bands). The *JHK* light and *J – H* colour curves folded on the period  $P=24.819$  d and on nearly twice the period  $P=49.690$  d are shown in Fig. 6.

The *JHK* phase curves are similar in shape showing a rapid rise to maximum and gentle slope. The phase curves folded on twice the period demonstrate the pattern of minima alternating in depth which is typical for the RV Tau type variables. The *J – H* colour reaches maximum at maximum light, so, the star is redder when brighter.

A brief summary of characteristics yielded from the photometric study, namely, the periods derived for different photometric bands as well as maximum brightness, peak-to-peak amplitudes, and the number of observations ( $N$ ), is given in Table 4.

The data presented in Table 4 and Fig. 7 indicates that the oscillation amplitude is the largest in the *U*-band, decreases with increasing wavelength in the optical range up to the

<sup>1</sup> <http://vgoranskij.net/software/WinEFrusInstruction.pdf>

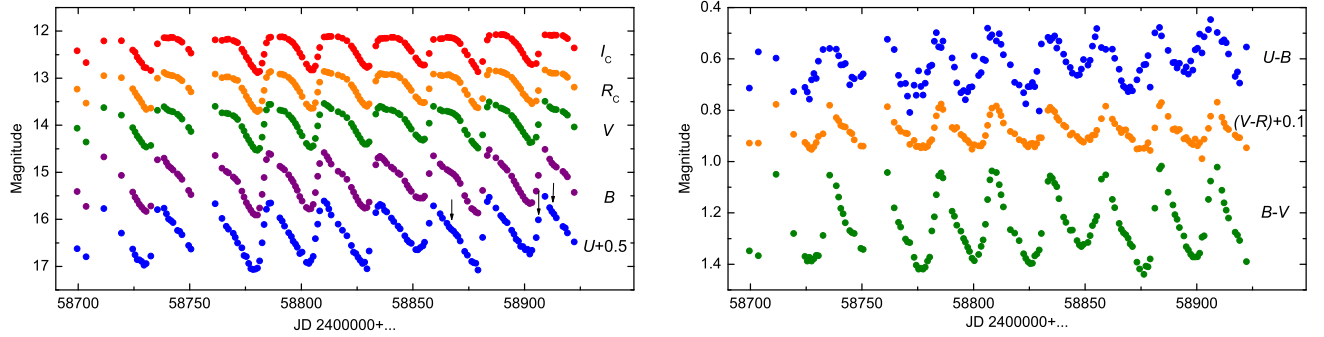


**Figure 2.** The  $UBVR_CI_C$ -band light and colour curves covering the period from August 2019 to March 2020.

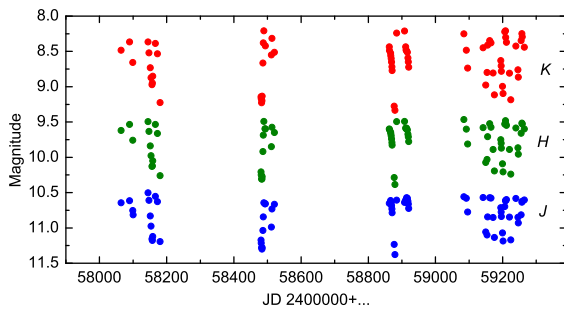


**Figure 3.** The  $JHK$ -band light curves covering the period from 2017 November to 2021 February.

$I_C$ -band, and then begins to increase in the near-IR range from  $J$  to  $K$ . The ratio of  $A(K)$  to  $A(V)$  is 1.08. This is an unexpected result, since in pulsating variables the amplitudes of oscillations in the near-IR range are usually lower than in the optical. For example, in classical Cepheids with periods  $P > 20$  d, the ratios of the amplitudes  $A(J)$ ,  $A(H)$  and  $A(K)$  to  $A(V)$  are approximately 0.4 (Inno et al. 2015). As we show below, IRAS 02143+5852 exhibits a significant excess of near-IR emission. As almost half of the  $H$ -band emission arises from dust and pulsations do affect the emission from the dust envelope, it seems credible to relate the observed near-IR-amplitude–wavelength dependence to the presence of dust.

### 3.2 Colour-colour diagrams

The location of IRAS 02143+5852 in the  $U-B$ ,  $B-V$  colour-colour diagram is shown in Fig. 8 along with the sequence of supergiants from Straižys (1982). The observed colours vary from the reddest in minimum light to the bluest in maxima which is common to temperature oscillations related to pulsations. Analysing spectroscopic data (see Section 4), we

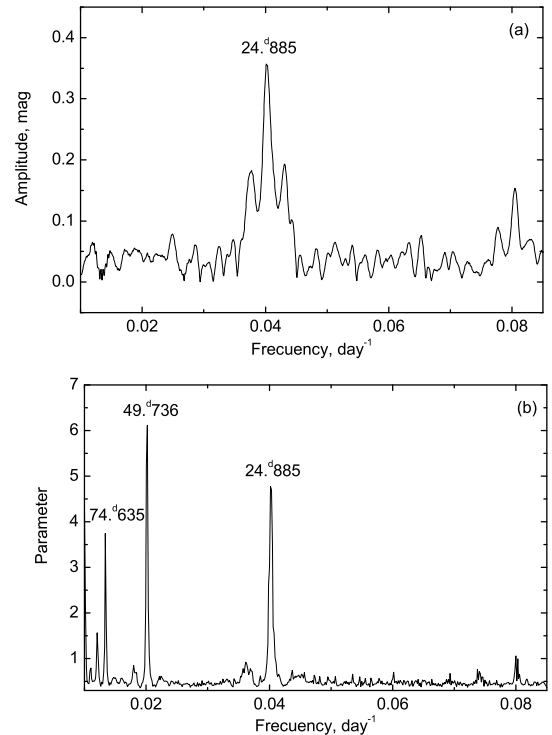


**Figure 4.** Frequency spectra for  $V$  data obtained by the Deeming (a) and Lafler-Kinman (b) methods. In the bottom panel, Parameter =  $1/\theta$  is plotted along the ordinate axis, where  $\theta$  is the normalised sum of the squares of the deviations of each subsequent point from the previous point in the light curve with a trial period.

found that at light maximum the star has a spectral class of approximately F0I, for which the normal colour index is  $(B-V)_0 = 0.20$  mag (Straižys 1982). The observed colour at light maximum is  $B-V = 1.03 \pm 0.02$  mag, and therefore the colour excess can be estimated as  $E(B-V) = 0.83 \pm 0.02$  mag.

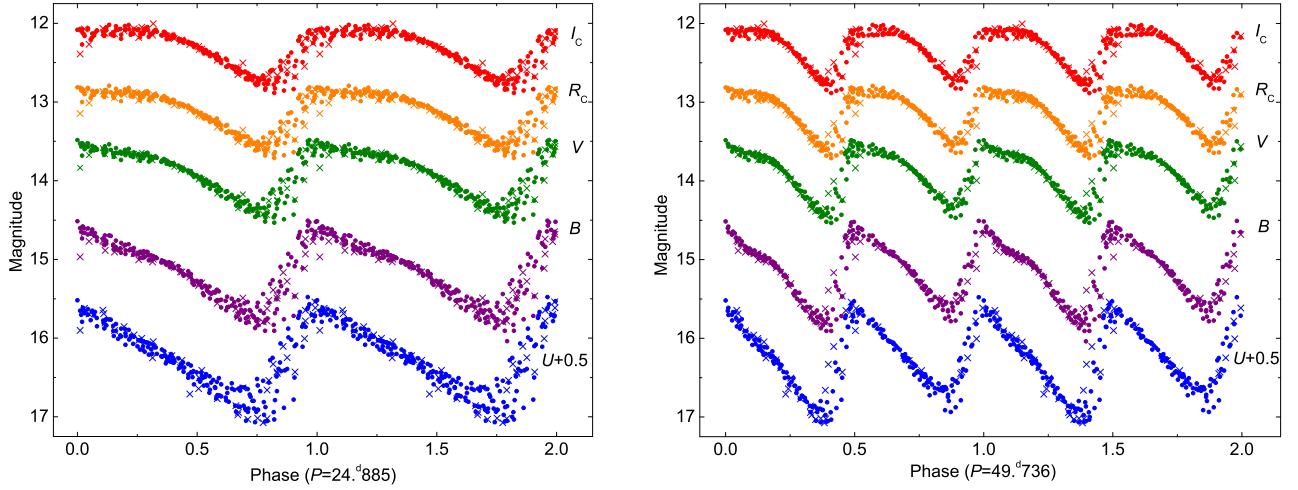


**Figure 5.** The  $UBVR_CI_C$  light curves folded on the periods of 24.885 d (left panel) and 49.736 d (right panel). Filled circles represent the CMO data, crosses – the data obtained in Slovakia.

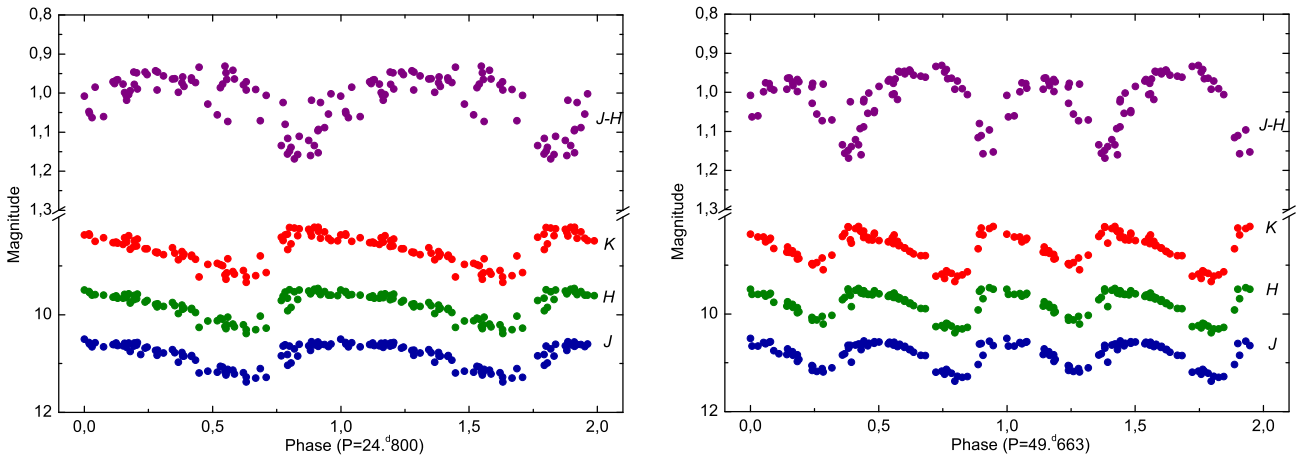


**Figure 6.** The  $JHK$  light and  $J-H$  colour curves folded on the periods of 24.793 d (left panel) and 49.690 d (right panel).

In the colour-colour diagram (Fig. 8), the dereddened colours are located above the sequence of supergiants, indicating that the star has some ultraviolet excess, which is typical of W Vir stars and may be due to low metallicity (Straižys 1982). As we discuss below, IRAS 02143+5852 also has low metal content.

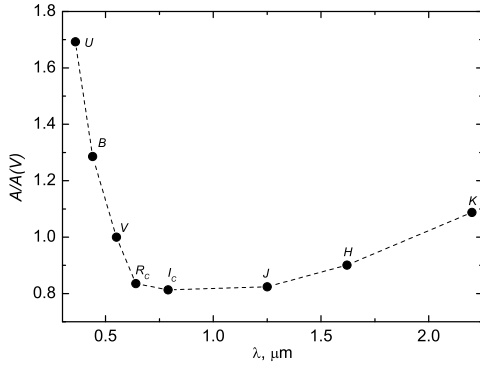
The star demonstrates a significant near-IR excess. In Fig. 9 we plot the  $J-H$ ,  $H-K$  colour-colour diagram for IRAS 02143+5852, the supergiant sequence from A5 to M5 and a blackbody with temperature in the range from 1200 to

2000 K. The  $J-H$  and  $H-K$  colours for supergiants were taken from Koornneef (1983) and converted to the 2MASS system using equations from Carpenter (2001) and then to the MKO-NIR system using equations from Leggett et al. (2006). The star's colours dereddened with  $E(B-V) = 0.83$  mag occupy the location which can be attributed to a sum of radiation from a  $\sim F5$  supergiant and hot dust with  $T_{\text{dust}} \sim 1300$  K. Note that the dust contribution is bigger in maximum light than in minimum.

The star also has a considerable excess of far-IR radiation

**Table 4.** Summary of the photometric study of IRAS 02143+5852 in 2018–2021.

Band	Brightness of maximum (mag)	Peak-to-peak amplitude (mag)	$P$ (days)	$N$
$U$	15.09	1.54	24.885	251
$B$	14.64	1.17	24.885	251
$V$	13.55	0.91	24.885	251
$R_C$	12.87	0.76	24.885	251
$I_C$	12.12	0.74	24.885	251
$J$ (MKO-NIR)	10.54	0.75	24.819	73
$H$ (MKO-NIR)	9.49	0.82	24.793	73
$K$ (MKO-NIR)	8.21	0.99	24.793	73

**Figure 7.** The ratio of the amplitude in  $UBVR_C I_C JHK$ -bands to the amplitude in the  $V$ -band.

related to cold dust. We present the circumstellar dust shell modelling in Section 6.

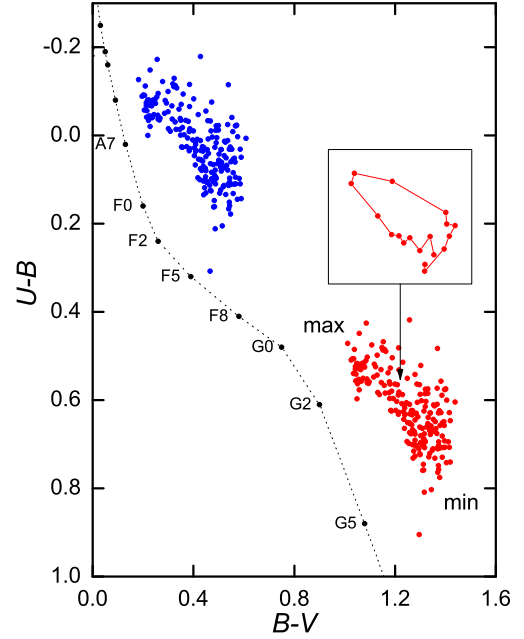
#### 4 SPECTRAL FEATURES AND STELLAR PARAMETERS

The flux-calibrated spectrum obtained on 2018 October 20 near the maximum brightness ( $\phi = 0.07$ ) is shown in Fig. 10. Because of low resolution in the short wavelength region most of lines are blended, which makes the analysis difficult. The most prominent details in the spectrum are the emission lines:  $H\alpha$ ,  $Ba\text{ II } \lambda 6496.9$ ,  $He\text{ I } \lambda 10830$  and  $P\alpha\beta$ . The  $H\beta$  line has also an emission component.

The main absorption features are D  $Na\text{ I}$ , diffusion interstellar bands (DIBs) at  $\lambda 5780$  and  $\lambda 6280$ , the  $O\text{ I}$  triplet at  $\lambda\lambda 7771\text{--}74$ , the  $Ca\text{ II}$  triplet ( $\lambda\lambda 8498, 8542, 8662$ ), the Paschen hydrogen lines, in particular P12, P14, P17, and the Brackett hydrogen lines.

The equivalent widths ( $EW$ s) of the most prominent lines are presented in Table 5. We consider  $EW$  negative for absorption and positive for emission. The measurement error is estimated to be about 10 per cent.

We have estimated  $T_{\text{eff}}$  and  $\log g$  of the star, using empirical relations from Molina (2018) and Mantegazza (1991). Molina

**Figure 8.**  $U-B$ ,  $B-V$  colour-colour diagram. Red and blue dots are observed and dereddened with  $E(B-V)=0.83$  mag data, respectively. The supergiant theoretical sequence is plotted with black dots connected by dotted line. In the inset, the data for one pulsation cycle (JD2458870.2–2458896.2) are shown.**Table 5.** Equivalent widths of absorption and emission lines in spectrum obtained on 2018 October 20.

$\lambda_{\text{lab}}$ (Å)	Identification	$EW$ (Å)
6496.9	$Ba\text{ II}$	0.53
6563	$H\text{ I}$	3.20
7771-74	$O\text{ I}$	-1.41
8469	P17	-1.18
8498	$Ca\text{ II}$	-1.85
8542	$Ca\text{ II}$	-2.23
8600	P14	-1.55
8662	$Ca\text{ II}$	-2.28
8753	P12	-1.73
10830	$He\text{ I}$	1.33
12818	$P\beta$	2.67

(2018) proposed a functional relationship to assess the value of  $\log g$ :

$$\log g = (2.20 \pm 0.20) - (0.58 \pm 0.13)(EW(O\text{ I})), \quad (2)$$

where  $EW(O\text{ I})$  is the equivalent width of the  $O\text{ I}$  triplet lines at  $\lambda\lambda 7771\text{--}74$ . For IRAS 02143+5852 we have derived  $\log g = 1.38 \pm 0.38$  which corresponds to the Iab luminosity class according to the calibration of Straižys (1982). But it is necessary to keep in mind that the strength of the  $O\text{ I}$

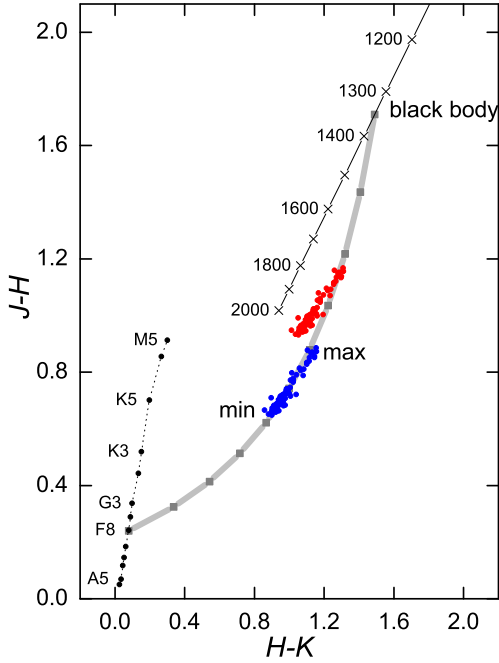


**Figure 9.**  $J-H, H-K$  colour-colour diagram. Red and blue dots are observed and dereddened with  $E(B-V) = 0.83$  mag data, respectively. The solid black line shows the loci of a blackbody with temperature ranging from 1200 to 2000 K. The dotted black line shows the supergiant sequence. The grey squares connected by a thick grey line correspond to a combination of an F8I star and a 1350 K blackbody, where each square is calculated with a step of 0.1 in terms of the fractions of contributions from individual components to the total emission in the  $H$ -band.

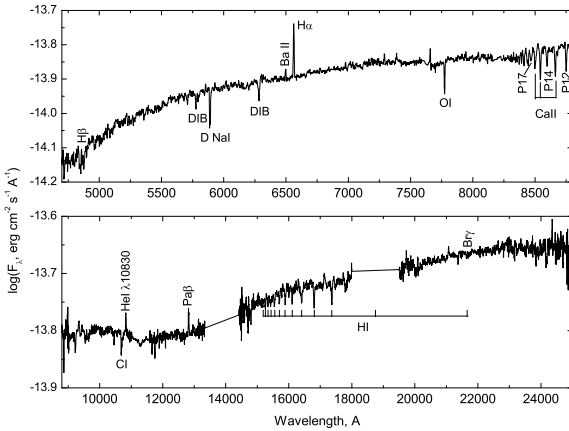


**Figure 10.** The flux-calibrated low-resolution spectrum taken at the Lick Observatory covering 4700–25000 Å. The main spectral features are indicated.

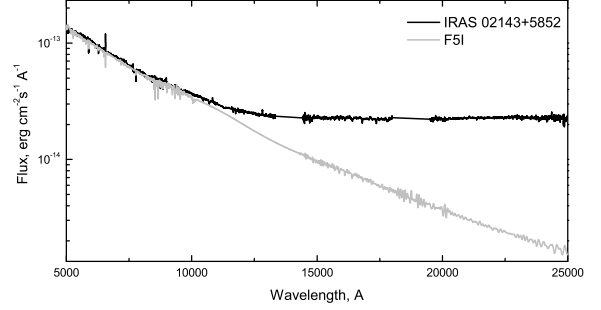


**Figure 11.** The Lick Observatory spectrum dereddened with  $E(B-V) = 0.83$  mag (black line) and the synthetic spectrum of an F5I star taken from Pickles (1998) (grey line).

triplet lines also depends on other atmospheric parameters (Kovtyukh et al. 2011), particularly on metallicity, which can be defined reliably only via the analysis of high-resolution spectra.

As was shown by Mantegazza (1991), the ratio  $Ca/P$  where  $Ca$  is the sum of  $EW$ s of the Ca II IR triplet lines and  $P$  is the sum of  $EW$ s of P12, P14, and P17, can be used to estimate the effective temperature of a star. Just as was reported by Mantegazza (1991) for the spectra of RV Tau stars, the components of the Ca II IR triplet are blended with P13, P15, and P16 in our spectra. Table 5 reports the measured  $EW$ s of P12, P14, P17 and Ca II triplet lines. In accordance with eq. 1 from Mantegazza (1991),

$$\log T_{\text{eff}} = 3.90 - 0.20 \log(Ca/P) \pm 0.07, \quad (3)$$

we derived  $T_{\text{eff}} = 7400^{+1248}_{-1152}$  K.

The calibration of Flower (1996) ascribes the intrinsic colour  $(B-V)_0 = 0.20$  mag to a supergiant with  $T_{\text{eff}} = 7400$  K. Our spectrum was obtained near maximum light when the mean value of  $B-V$  is about 1.03 mag, so, the colour excess can be estimated as 0.83 mag. The spectrum dereddened with  $E(B-V) = 0.83$  mag is shown in Fig. 11 together with the synthetic spectrum of an F5I star taken from the stellar spectral flux library presented by Pickles (1998). As one can see, the 5000–7500 Å spectrum of IRAS 02143+5852 corresponds well to an F5I type spectrum, whereas at longer wavelengths there is a significant excess of radiation compared to a standard star. According to the calibration of Flower (1977), an F5I star has the temperature  $T_{\text{eff}} = 7000$  K which falls within the range of temperatures inferred from the  $Ca/P$  ratio.

We were interested to study spectral changes depending on the pulsation phase. So, we obtained 12 spectra in the 3500–7500 Å range at different pulsation phases on the 2.5-m telescope of CMO with TDS (Table 3). The main characteristics of the IRAS 02143+5852 spectrum are the following:

- The optical spectrum is dominated by the Balmer lines.  $H\alpha$  and  $H\beta$  have emission components which vary with pulsation phase. The  $H\alpha$  emission appears near minimum light, persists on the rising branch until maximum and then weakens rapidly on the declining branch and becomes double-

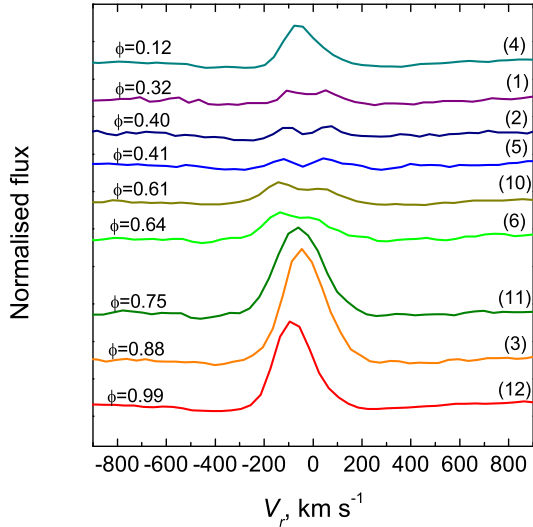


**Figure 12.** The evolution of the  $H\alpha$  profile with pulsation phase. The numbers in parentheses indicate the order number of spectra as it is defined in Table 3.

peaked with a peak-to-peak separation of about  $3.6 \text{ \AA}$  or  $164 \text{ km s}^{-1}$ .

Strong hydrogen emission lines observed during rising light are characteristic of population II Cepheids and their appearance is explained by the propagation of a shock wave through the expanding outer layers of stellar atmosphere (Abt 1954; Whitney 1956; Wallerstein 1959).

- In the blue part of the spectrum there are molecular bands of CH ( $\lambda 4261$ ,  $\lambda 4280$ ,  $\lambda 44323$ ) and CN ( $\lambda 4197$ ,  $\lambda 4214$ ,  $\lambda 4216$ ). The strength of the bands varies with pulsation phase and is the largest near the middle of the declining branch. Fig. 13 shows the blue spectral region with the molecular bands mentioned above.

IRAS 02143+5852 is found to have weaker metal lines in its spectrum compared to stars of normal metallicity. In order to illustrate this fact, we show the spectra of IRAS 02143+5852 obtained near minimum and maximum light as well as the spectra of HD 17971 (F5Ib) and SAO 37370 (F0Ib) obtained with TDS, so, all of them have the same spectral resolution.

We have also compared the spectrum of IRAS 02143+5852 with that of the star CC Lyr, which is a Type II Cepheid (Harris 1985). It has the pulsation period  $P = 24.01 \text{ d}$  (Berdnikov et al. 2020) which is close to that of IRAS 02143+5852. In Fig. 14 we present the spectrum of CC Lyr which we obtained on 2020 March 8 when the star was on the ascending branch of light curve ( $\phi = 0.76$ ). The spectrum has much in common with that of IRAS 02143+5852: the appearance of the Balmer series is nearly the same, the metal lines are also weak. Like IRAS 02143+5852, CC Lyr displays strong  $H\alpha$  emission and the CH band at  $\lambda 4280$ .

Harris and Wallerstein (1984) noted that ‘because of their peculiarities, the spectra of Type II Cepheids are difficult to classify by direct comparison with MK standards’. Based on HI lines Harris and Wallerstein (1984) ascribed an F4-

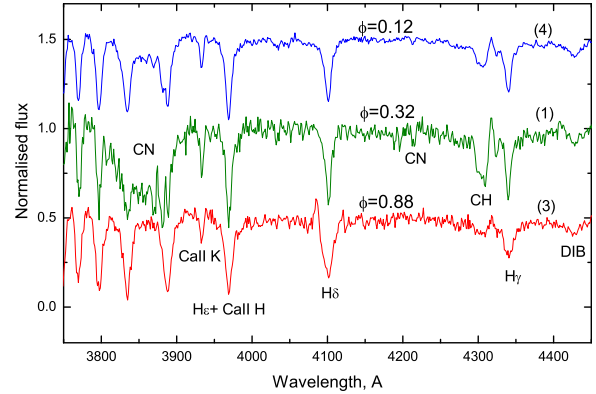


**Figure 13.** The spectrum in the  $3750\text{--}4450 \text{ \AA}$  wavelength range at different pulsation phase. The numbers in parentheses correspond to the order number of spectra as it is defined in Table 3.

F8 spectral type to CC Lyr depending on the pulsation phase; from metal lines they deduced an A type and also pointed to the presence of the CH band. So, according to Harris and Wallerstein (1984) the spectral classification of CC Lyr at maximum light is hF4mA:CH+1. We can state that the spectra of IRAS 02143+5852 and CC Lyr are similar in their peculiarity.

## 5 LUMINOSITY, DISTANCE AND EVOLUTIONARY STATUS

IRAS 02143+5852 shows many important similarities to long-period Type II Cepheids, e.g., the shape of light curves, the pulsation period, the emergence of Balmer emission, among other observed photometric and spectroscopic properties. We therefore decided to estimate the star’s luminosity from the period-luminosity relation established for this type of pulsating variables. We applied the relation  $M_V = -0.61 - 2.95 \log P + 5.49(V - R)_0$  proposed by Alcock et al. (1998) for the long-period ( $0.9 < \log P < 1.75$ ) Type II Cepheids.

The mean observed colour of IRAS 02143+5852 is  $B - V = 1.25 \pm 0.11 \text{ mag}$ . After correcting for reddening with  $E(B - V) = 0.83 \text{ mag}$  we have  $(B - V)_0 = 0.42 \text{ mag}$  which corresponds to  $(V - R)_0 = 0.39 \text{ mag}$  according to the calibration of Straižys (1992). This value of  $(V - R)_0$  leads to  $M_V = -2.64 \text{ mag}$ . Accounting for bolometric correction  $BC = -0.007 \text{ mag}$  (Flower 1996) we derive  $M_{\text{bol}} = -2.65 \text{ mag}$  and  $\log L/L_\odot = 2.95$ .

As IRAS 02143+5852 is positioned as a post-AGB star, let us compare the parameters of the star with the predictions inferred from the evolution models for post-AGB objects presented by Miller Bertolami (2016). Typical post-AGB objects with initial masses on the Zero Age Main Sequence (ZAMS) between  $0.8$  and  $8.0 M_\odot$  at the stage after shedding their shells on AGB have final masses of  $0.52\text{--}0.85 M_\odot$  and luminosities  $\log L/L_\odot$  ranging from  $3.4$  to  $4.2$ , respectively, which is significantly higher than that obtained for IRAS 02143+5852.

Taking into account the new data presented here and our



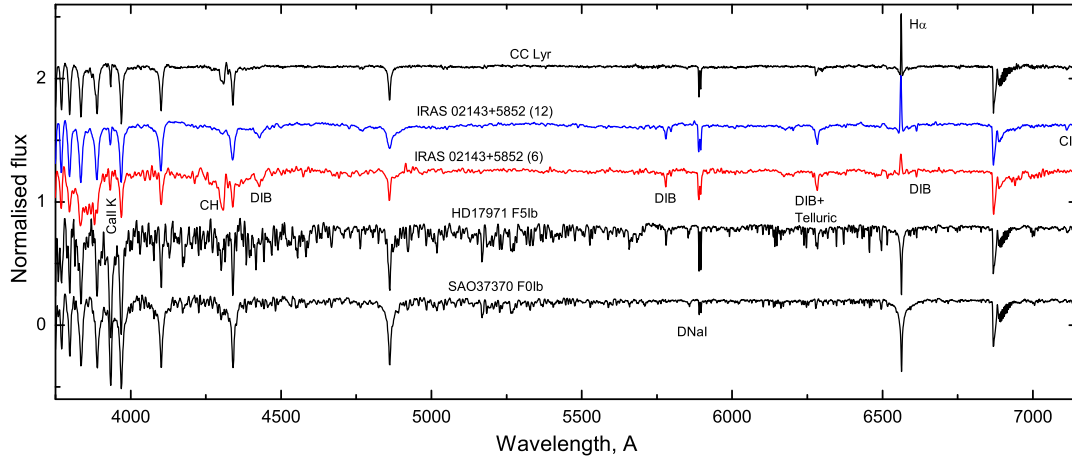


**Figure 14.** The spectra of IRAS 02143+5852 at two phases of pulsation cycle – near the minimum (6) and near the maximum (12) light – and the spectra of HD 17971 (F5Ib), SAO 37370 (F0Ib) and CC Lyr. The spectra are normalised to continuum and arbitrarily shifted along the vertical axis.

presumption of IRAS 02143+5852 being a W Vir star, we have turned to the evolutionary models of W Vir pulsating variables. The evolutionary status of these stars was discussed more than once, e.g., by [Gingold \(1974, 1976\)](#). [Gingold \(1985\)](#) and [Fadeyev \(2020\)](#) summarized the previous work done in this area. On the basis of self-consistent stellar evolution models and nonlinear stellar pulsation calculations, [Fadeyev \(2020\)](#) concluded that W Vir pulsating variables are the low-mass post-AGB stars that experience the final helium flash. He found that a set of evolutionary models with masses  $M = 0.536M_{\odot}$ ,  $0.530M_{\odot}$  and  $0.526M_{\odot}$  that experience the loop in the Hertzsprung-Russel diagram, due to the final helium flash, can provide a solution of hydrodynamic equations which describes radial oscillations of W Vir stars. The  $\log L/L_{\odot} = 2.95$  found for IRAS 02143+5852 falls into the range of luminosities predicted for the above masses.

The results of the Gaia mission for IRAS 02143+5852 are confusing. The parallax of the star listed in the Gaia DR2 turned out negative ( $\pi = -0.8487 \pm 0.4583$  mas; [Gaia Collaboration \(2018\)](#)). The distance based on these data is  $d = 3606^{+2032}_{-1331}$  pc ([Bailer-Jones et al. 2018](#)). The parallax  $\pi = 1.3637 \pm 0.2892$  mas introduced in the Gaia DR3 ([Gaia Collaboration 2022](#)) brings the star much closer to us. The distance estimate for this parallax is  $d = 854^{+276}_{-175}$  pc ([Bailer-Jones et al. 2021](#)). At this distance, the star would have had a luminosity of about  $16L_{\odot}$ , however, which contradicts its evolutionary status.

## 6 THE MODEL OF THE CIRCUMSTELLAR DUST ENVELOPE AND MODELLING ASPECTS

The SED of the object demonstrates a prominent IR excess. Thus, assuming that the excess is caused by the radiation from heated dust, we estimated the circumstellar

dust envelope parameters via the simulations with RADMC-3D ([Dullemond et al. 2012](#)).

Our modelling was based on the following sets of observational data:

- *UBVR<sub>c</sub>I<sub>c</sub>JHK* photometry. We used the absolute flux calibrations from [Straizys \(1992\)](#) for the *U*, *B*, *V* bands, [Bessell \(1979\)](#) for the *R<sub>c</sub>*, *I<sub>c</sub>* bands and [Tokunaga & Vacca \(2005\)](#) for the *J*, *H*, *K* bands.
- The observed fluxes at 65 and 90  $\mu\text{m}$  from the AKARI/FIS Bright Source Catalogue. The data at 140 and 160  $\mu\text{m}$  were omitted because of their low quality.
- The observations at 9 and 18  $\mu\text{m}$  from the AKARI/IRC Point Source Catalogue.
- The *W1*, *W2*, *W3*, and *W4* magnitudes from the All-WISE Data Release [Cutri et al. \(2013\)](#). The fluxes were calibrated according to [Jarrett et al. \(2011\)](#).
- The flux densities in the *A*, *C*, *D*, and *E* bands of the *Midcourse Space Experiment (MSXC6)*.
- The average non-colour corrected flux densities at 12, 25 and 60  $\mu\text{m}$  from the IRAS Point Source Catalog v2.1 (PSC). The data at 100  $\mu\text{m}$  were excluded as only the upper limit is presented.

We modelled the SED of the star using our *UBVR<sub>c</sub>I<sub>c</sub>JHK* data for maximum light and the data available from different catalogues listed in Table 6. We used the initial model atmosphere parameters  $T_{\text{eff}} = 7460$  K and  $\log g = 1.38$  found in this study which correspond to an F5I star from [Pickles \(1998\)](#). An example of the fitting SED derived for IRAS 02143+5852 is shown in Fig. 15.

The object is situated close to the galactic plane with the galactic latitude of about  $-2^{\circ}$ . According to [Bailer-Jones et al. \(2018\)](#) the distance to the object is within the confidence interval of about 2272–5636 pc. These two facts lead to large interstellar extinction which distorts the spectral energy distribution of the object.

**Table 6.** Photometric data used to construct the SED for IRAS 02143+5852.

Telescope	Wavelength ( $\mu\text{m}$ )	Flux (Jy)	Obs. time	Reference
WISE	3.4, 4.6, 12, 22	0.586, 0.836, 5.685, 13.803	2010	Cutri et al. (2013)
AKARI PSC	9, 18	3.712, 9.705	2006-2007	Murakami et al. (2007)
AKARI BSC	90, 140, 160	2.697, 1.297, 0.361	2006-2007	Murakami et al. (2007)
IRAS	12, 25, 60	5.9, 18.1, 5.39	1983	Helou and Walker (1988)
MSX	8.28, 12.13, 14.65, 21.34	3.67, 5.117, 6.044, 15.62	1996	Egan et al. (2003)

A distance estimation error causes an uncertainty in the SED corrected for interstellar extinction. We decided to use the period-luminosity relation for W Vir variables (Alcock et al. 1998) to estimate the distance to the object. Our approach to this problem allowed us to reconcile the luminosity derived from this relation, distance to the star and the luminosity calculated by integrating the SED corrected for interstellar extinction.

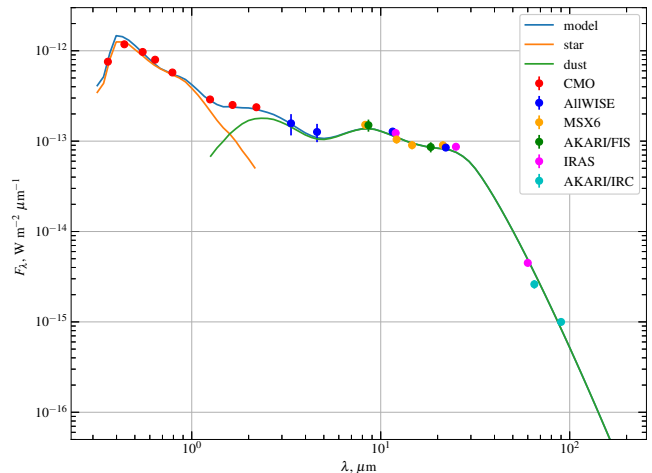
This method is as follows. The period-luminosity relation, when averaged over the period, gives a bolometric magnitude of  $-2.65$  mag, corresponding to a luminosity of  $910 L_{\odot}$ . Comparing the bolometric magnitude to the actual observations yields a distance of 2470 pc.

To take into account interstellar extinction we used dust maps by Green et al. (2019) and the interstellar extinction law from Cardelli et al. (1989) and O'Donnell (1994) assuming  $R_V = 3.1$  as a mean for the Galaxy.

To estimate the distance we applied the photometry averaged over the period and assumed that the fluxes corresponding to the *AKARI*, *WISE*, *MSX* and *IRAS* data did not change essentially during the pulsation cycle. This assumption needs to be explained. It was shown by Fedoteva et al. (2020) for a Mira-type star V CrB that the main parameters of the model dust shell ( $\tau$ ,  $R_{in}$ ,  $R_{out}$  and dust properties) do not depend on whether the maximum or minimum light SED is fitted. V CrB varies with an amplitude of  $> 4$  mag in  $B$  and  $\sim 0.8$  mag in  $KLM$  and a period of 355.2 d, so, even if the case of such large-scale variations does not require different dust shell models for minimum and maximum light, we can assume the constancy of IR fluxes during the pulsation cycle for IRAS 02143+5852.

The temperature of the internal star is of great importance for simulating. Since we have the spectrum at maximum light obtained at the Lick Observatory we were able to evaluate the corresponding temperature. The value turned out to be roughly 7400 K. Thus, the SED modelling was carried out for the phase of the maximum brightness. This means that unlike the case of determining the distance when we considered the average SED, for the modelling we applied the photometry obtained at maximum light. We corrected these data for interstellar extinction using the distance estimated as was described above. As mentioned earlier, we presume that the fluxes corresponding to the *AKARI*, *WISE*, *MSX* and *IRAS* data do not change significantly during the pulsation cycle. So, we let ourselves adopt these observational data not only for the average brightness but also for the maximum light.

The SED of IRAS 02143+5852 has a non-trivial profile, such that the flat SED in the IR domain can not be explained by the presence of only one dusty spherical shell with a simple dust density distribution  $\rho \propto r^{-\alpha}$ . A series of simulations showed that in order to reproduce the observed SED

**Figure 15.** T

he SED of IRAS 02143+5852. The blue curve represents the resulting fit corresponding to the model described in the text, the orange one – the SED of the central star reprocessed by the dust, the green one is the radiation from the circumstellar dust shell. The symbols depict the observational data points. For some data the error bars are smaller than the size of the symbols.

we should consider at least three nested spherical layers that correspond to the different stages of mass loss. The idea of multiple shells has been supported by observational evidence for AGB stars (see, for example, the studies on CW Leo by Mauron & Huggins (2000) or Cernicharo et al. (2015)).

Thereby, following the law of parsimony, we considered three shells (three components of the composite dust envelope) in further modelling, which was carried out under the following assumptions:

- The SED of the star is assumed to be that of an F5I star.
- The components of the circumstellar dust envelope are spherical layers located symmetrically about the star.
- $\alpha = 2$  for each spherical shell, since this describes the simplest case of the constant mass-loss rate and expansion velocity.
- Dust grains are spherical. Hence, the opacity coefficients were calculated in accordance with the Mie theory.
- Since there is no indication of the chemical composition, we used amorphous carbon dust grains to avoid additional ambiguity. The corresponding optical constants were taken from Suh (2000).

Fig. 15 represents the best-fitting model SED with minimal normalized deviations from the observed data.

The parameters of the corresponding model dust shells,

namely, the distance from the stellar center to the inner and outer boundaries, the radius of dust grains, the optical depth, the dust mass and the mass-loss rate, are listed in Table 7.

Our estimates of the mass-loss rate were derived under the assumption that the expansion velocity and the gas-to-dust ratio are equal by the order of magnitude to the typical values found for the circumstellar envelopes of AGB stars:  $v_e=10 \text{ km s}^{-1}$  and  $\rho_g/\rho_d=100$ . Our mass-loss rate estimates are in agreement with the values that were derived for AGB stars from observations and fall within the interval  $\sim 10^{-8} - 10^{-5} M_\odot \text{ yr}^{-1}$  (see Ramstedt et al. (2009)). Fig. 16 demonstrates the model density distribution in the dust envelope. The discontinuities coincide with the boundaries between different components of the dust envelope.

### 6.1 Verification of unambiguity

To judge whether a two or three-shell model fits the observed data better, we used the  $F$ -test to select the most appropriate model at a significance level of  $\alpha = 5\%$ . We could not construct a model consisting of one or two dust shells which could reproduce the observed SED, for no combination of parameters did we get the  $F$  value less than critical.

Our simulation is not based on analytical formulae, so, it is rather problematic to claim the confidence intervals of the obtained model parameters. If we consider a three-shell model, then, in our case, for a limited sample of independent parameters and observed data points the critical value of  $F$ -test statistics is  $F(5\%) = 2.5$ . Our best model has  $F = 1.25$ . We used the  $F$ -test to estimate the interval for each parameter where  $F < 2.5$ . So, we successively varied each of model parameters with the others being fixed until  $F$  was less than 2.5. Then we considered the range between derived extreme values as a confident interval for that parameter. The corresponding  $F$  values for each variation are shown in Fig. 17. The derived intervals for all model parameters are listed in Table 7. One can see that the most strictly constrained parameters are  $r_2$  and  $r_3$ , in the sense that a slight relative variation significantly affects the shape of SED, whereas  $r_4$ , the outer radius of dust envelope, has the least effect: even a three time increase keeps  $F < 2.5$ . This can be understood if we turn to the aspects of modelling: with  $\tau_3$  being fixed, an increase in  $r_4$  leads to a decrease in the dust temperature at the outer radius ( $r_4$ ) and to some redistribution of matter inside the outer shell, so, that the dust density at its inner radius  $r_3$  declines only slightly, thus barely affecting the shape of SED. An increase of far-IR emission produced by cold dust at a new larger  $r_4$  is partially compensated by a decrease of dust density at the previous distance  $r_4$ .

The variation of model parameters affects the total mass of the dust envelope differently. We calculated the total dust mass for each model that satisfied the criterion  $F < 2.5$ . Fig. 18 visualizes how the  $F$  value changes with the change of the outer dust shell mass caused by the variation of one of model parameters, namely those corresponding to the outer shell:  $r_3$ ,  $r_4$  – its inner and outer radii,  $\tau_V$ . It is clearly seen that the dust mass strongly depends only on the outer radius. Other parameters modify the SED but barely affect the total dust mass.

Our calculations show that the shell radius does not affect the derived mass-loss rate, even though it does affect the resulting mass. It is due to the fact that the lifetime of the

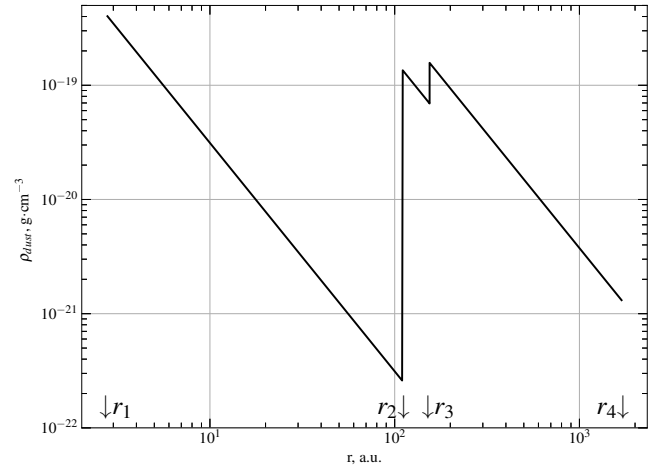


**Figure 16.** The model dust density distribution in the envelope plotted on logarithmic scale. The values  $r_1$ ,  $r_2$ ,  $r_3$  and  $r_4$  – the boundary positions of the dust envelope components.  $r_1 = 2.5 \text{ au}$ ,  $r_2 = 110 \text{ au}$ ,  $r_3 = 146 \text{ au}$  and  $r_4 = 1750 \text{ au}$  according to Table 7 where the model parameters are listed.

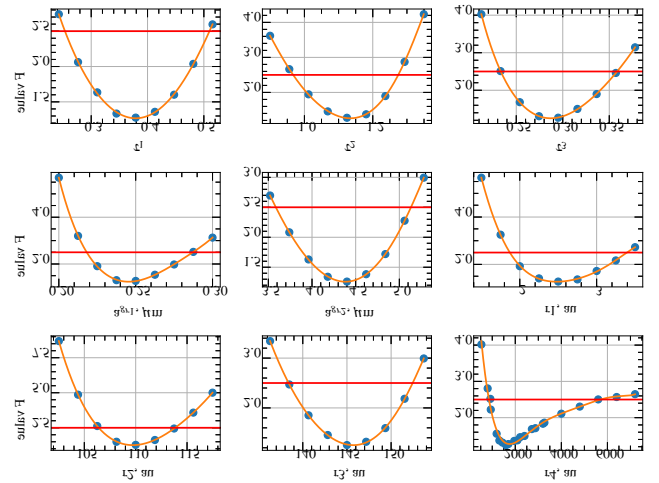


**Figure 17.** The plot illustrating the process of deriving confidence intervals for model parameters. Each panel shows how the  $F$  value changes with one single parameter being varied and the others being fixed. The red line indicates the critical  $F$  value.

shell and its mass grow linearly with radius, if we assume  $\rho(r) \sim r^{-2}$ .

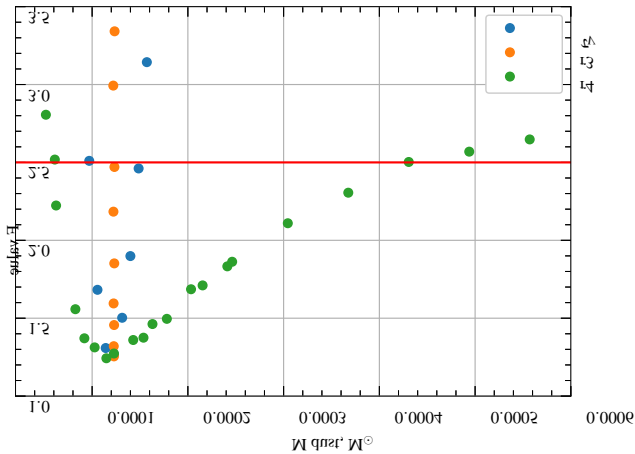
### 6.2 The necessity of large dust grains

The main peculiarity of this model is the presence of large dust grains with a radius of  $5 \mu\text{m}$  in the third shell. The usage of such large particles is dictated by the necessity to reproduce the SED in the  $25 \mu\text{m}$  region.

Carbon dust grains with a radius of  $\sim 1 \mu\text{m}$  have a larger absorption opacity coefficient at  $25 \mu\text{m}$  than the smaller ones with  $a_{\text{gr}} \sim 0.1 \mu\text{m}$ . At the same time, the absorption opacity coefficient of the larger grains with  $a_{\text{gr}} \sim 1 \mu\text{m}$  is much smaller in the optical region than that of the smaller ones with  $a_{\text{gr}} \sim 0.1 \mu\text{m}$ . Hence, when we try to reproduce the

**Table 7.** The parameters of the model dust envelope components.

	№1	№2	№3
Inner edge, au	$2.5^{+0.9}_{-0.6}$	$110^{+4}_{-3}$	$146^{+7}_{-7}$
Outer boundary, au	$110^{+4}_{-3}$	$146^{+7}_{-7}$	$1750^{+3900}_{-900}$
Dust grain radius, $\mu\text{m}$	$0.25^{+0.04}_{-0.03}$	$0.25^{+0.04}_{-0.03}$	$4.4^{+0.7}_{-0.8}$
Optical depth, $\tau_V$	$0.38^{+0.13}_{-0.13}$	$1.12^{+0.15}_{-0.16}$	$0.3^{+0.06}_{-0.06}$
Dust mass, $M_\odot$	$7^{+2.3}_{-2.2} \times 10^{-9}$	$1.2^{+0.3}_{-0.2} \times 10^{-6}$	$1.1^{+3}_{-0.5} \times 10^{-4}$
Mass-loss rate, $M_\odot\text{yr}^{-1}$	$1.7 \times 10^{-8}$	$6.8 \times 10^{-6}$	$1.1 \times 10^{-5}$

**Figure 18.** The plot illustrating the change of the outer shell mass and corresponding  $F$  value due to variation of one of the outer shell parameters  $\tau_V$ ,  $r_3$ ,  $r_4$  with the rest being fixed.

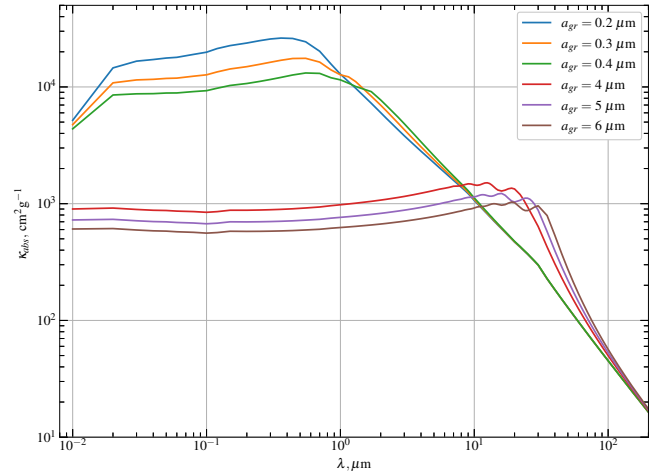
SED in the  $25\ \mu\text{m}$  region using the dust grains with the radius smaller than  $5\ \mu\text{m}$ , a large mass of dust that is required for this will cause too much absorption in the optical range. But in the case of the particles with a radius of  $5\ \mu\text{m}$  the values of absorption and reradiation caused by the third dust shell component are consistent with the observed SED. The absorption opacity coefficients for dust grains of different sizes are depicted in Fig. 19.

### 6.3 A short discussion on the dust grain sizes

As a result of our research two populations of dust grains were found: smaller grains with  $a_{\text{gr}} = 0.3\ \mu\text{m}$  and larger ones with  $a_{\text{gr}} = 5\ \mu\text{m}$ .

The radius of small grains we found here coincides, in order of magnitude, with the sizes of dust particles claimed by the recent observational and theoretical studies. Dust grains of the similar radii were detected by Norris et al. (2012) ( $a_{\text{gr}} \sim 0.3\ \mu\text{m}$ ) for several O-rich AGB stars and by Ohnaka et al. (2017) for W Hya ( $a_{\text{gr}}$  is about  $0.1\ \mu\text{m}$  at minimum light and  $0.5\ \mu\text{m}$  at maximum light). These results are in agreement with the theoretical models of Hofner (2008) who deduced that silicate dust grains of M-type AGB stars should have radii in the range of about  $0.1\text{--}1\ \mu\text{m}$  to drive the stellar outflow. In the case of C-type AGB stars where carbon species dominate, the modelling presented by Mattsson et al. (2010) shows that the dust with  $a_{\text{gr}} \sim 0.1\ \mu\text{m}$  may be common for stellar winds.

As for the large dust grains, there are some studies that

**Figure 19.** Mass absorption coefficient  $\kappa_{\text{abs}}$  for spherical amorphous carbon dust grains with different radii  $a_{\text{gr}}$ . The calculation was performed according to the Mie theory with the optical constants for amorphous carbon adopted from Suh (2000).

have found evidence for the presence of rather big dust particles in the circumstellar discs around the stars more evolved than IRAS 02143+5852. Jura (1997) proposed that there is an orbiting, long-lived gravitationally bound disk of dust grains with radii  $\geq 0.02\ \text{cm}$  surrounding a carbon-rich AGB star in the Red Rectangle nebula. Shenton et al. (1995) analysed the IRAS-millimetre flux distributions of the two post-AGB stars AC Her and 89 Her and suggested the existence of large grains ( $a_{\text{gr}} \geq 1\ \mu\text{m}$ ) in their dusty discs. De Ruyter et al. (2006) explored a sample of post-AGB stars and found the emission from large ( $\geq 0.1\ \text{mm}$ ) grains. They assumed that the presence of such large grains may be the indication of Keplerian discs around binary systems, where the grain growth is facilitated. Hence, according to these papers large dust grains around IRAS 02143+5852 is a possible indication of the second component which has not been discovered yet and the dusty disc surrounding the possible binary system.

## 7 DISCUSSION

Our photometric study has produced evidence that IRAS 02143+5852 is a pulsating variable with a period of about 25 d and light curves typical for W Vir stars. The star also demonstrates some similarity to the RV Tau stars, namely, a pattern of alternating minima observed in the  $U$

and *JHK* phase light curves. The double wave of alternating deep and shallow minima in the light curve of the RV Tau variables is their main characteristic. Gerasimović (1929) proposed that the recurring feature of alternating minima represents two pulsation modes simultaneously excited in a ratio of 2:1 resonance. A detailed description of this and other explanations for this phenomenon is presented by Pollard et al. (1996). It should be mentioned that much less pronounced period doubling behaviour has recently been discovered in some W Vir (Plachy et al. 2018), BL Her (Smolec 2012) and RR Lyr (Szabo et al. 2010) type stars.

We have found that hydrogen emission is present in the spectrum of IRAS 02143+5852 at certain phases of the pulsation cycle with H $\alpha$  being the most prominent. We have also detected the Ba II and He I  $\lambda$ 10830 emissions in the spectrum obtained close to maximum light.

Schmidt et al. (2004b) studied the H $\alpha$  and helium emissions in long-period (with periods longer than 8 days) Type II Cepheids. Kovtyukh et al. (2011) detected and investigated the behaviour of emission and line doubling of many metallic lines, in particular, Ba II, in the spectrum of the Type II Cepheid W Vir. Strong metallic emissions were observed in the spectra of the RV Tau stars U Mon and AC Her (Bopp 1984).

Pollard et al. (1997) reviewed the previous spectroscopic studies of the RV Tau variables and presented the results of a long-term photometric and spectroscopic study of eleven stars classified as RV Tau. In particular, they concluded that line emission originates within the de-excitation zone of the shock wave that propagates through the stellar atmosphere. The fact that H $\alpha$  is observed in emission for much of the pulsation cycle is due to a large range of atmospheric layers where this line forms. On the contrary, the metallic emissions appear only when the shock wave crosses the region where these lines originate. Thus, IRAS 02143+5852 with emission lines of hydrogen, helium, and metals in the spectrum is representative of W Vir and RV Tau stars.

Significant excesses of near, medium and far-IR radiation are distinguishing features of IRAS 02143+5852. These are due to multiple circumstellar envelope, which according to our simulations, has a complicated structure and was formed during three episodes of mass loss.

Many RV Tau stars have an IR-excess which indicates the presence of circumstellar material and for some of them a disc-like structure was proved. Moreover, as the discs are found around binaries, RV Tau stars are likely to be binary systems, too (Manick et al. 2017).

The near-IR excess is rare among W Vir stars. Using published data on periods and SEDs for the Galactic Type II Cepheids, Saario et al. (2018) found that only 43 objects of 1307 have a near-IR excess and only 8 of these 43 have periods less than 30 d.

Besides, IRAS 02143+5852 stands out among typical W Vir stars because of its location in the Galaxy. Whereas W Vir stars are low-mass pulsating variables of the intermediate disc or halo population, IRAS 02143+5852 lies near the Galactic plane ( $b = -1.^\circ 93$ ).

## 7.1 Objects analogous to IRAS 02143+5852

Among the W Vir stars with the longest periods and RV Tau stars with the shortest periods, there are few objects similar to IRAS 02143+5852.

**CC Lyr.** CC Lyr is classified in the General Catalogue of Variable Stars (GCVS) as a W Vir-type variable with  $P = 24.16$  d and a full peak-to-peak amplitude of  $\Delta V = 0.8$  mag (Samus et al. 2017).

The light curves of this star, as well as those of IRAS 02143+5852, show alternating minima of different depth, a characteristic of RV Tau variables (Schmidt et al. 2004a). CC Lyr, as well as IRAS 02143+5852, has a IR excess (Schmidt 2015), also invariably a characteristic of RV Tau variables. CC Lyr and IRAS 02143+5852 have similar spectra (see Section 4).

Maas et al. (2007) determined the parameters of the star  $T_{\text{eff}} = 6250$  K and  $\log g = 1.0$  and revealed that refractory elements show large depletion (e.g.,  $[\text{Fe}/\text{H}] = -3.5$ ). Aoki et al. (2017) confirmed its extremely low metallicity ( $[\text{Fe}/\text{H}] < -3.5$ ) and concluded that the abundance anomaly of this star is due to dust depletion. In addition, Aoki et al. (2017) found that the double-peaked H $\alpha$  emission shows no evident velocity shift which suggests that the emission is forming in the circumstellar matter, presumably the rotating disc around the object. The double-peaked H $\alpha$  emission is also observed in the spectrum of IRAS 02143+5852 at certain phases of the pulsation cycle.

So, IRAS 02143+5852 and CC Lyr are similar in showing alternating minima and in having close pulsation periods and composite spectra that combine the properties of a hot and a cool star. At the same time, IRAS 02143+5852 demonstrates a significantly larger IR excess than CC Lyr. Besides, they differ in their location in the Galaxy: whereas CC Lyr is a high galactic latitude star ( $b = +17.^\circ 27$ ), IRAS 02143+5852 lies close to the Galactic plane.

**AF Crt = IRAS 11472-0800.** According to GCVS it is a SRB-type variable (semiregular late-type giants with poorly defined periodicity) (Samus et al. 2017).

Kiss et al. (2007) determined a period of  $P = 31.5 \pm 0.6$  d based on the ASAS data and classified the star as a Population II Cepheid. Through analysing the photometric data obtained at the Valparaíso University Observatory (VUO) in 1995–2008 (Van Winckel et al. 2012) derived well-determined period values of  $31.16 \pm 0.01$  d ( $V$ ) and  $32.18 \pm 0.04$  d ( $R$ ) (Van Winckel et al. 2012).

We have analysed the ASAS-SN data (Shappee et al. 2014; Kochanek et al. 2017) in the  $V$ -band obtained from 2012 to 2018 and determined a period of  $P = 31.7$  d and a peak-to-peak amplitude of  $\Delta V = 0.8$  mag. The light curves look like that of a W Vir star, but the period lies in the range typical for RV Tau stars. Besides, the photometric data folded on twice the period demonstrate the alternation of more and less deep minima as is common for RV Tau.

AF Crt, as well as CC Lyr, is located at high galactic latitude ( $b = +51.^\circ 56$ ). It is an extremely depleted object with the photospheric abundances of  $[\text{Fe}/\text{H}] = -2.7$  and  $[\text{Sc}/\text{H}] = -4.2$  (Van Winckel et al. 2012). Van Winckel et al. (2012) also found that besides the variation of radial velocity related to pulsations, there is a long-term systematic change which they attributed to binary motion.

AF Crt is a highly evolved star of spectral type F, with

a large IR excess produced by thermal radiation of circumstellar dust. Based on all the data known to date, [Van Winckel et al. \(2012\)](#) concluded that AF Crt is a low-luminosity analogue of the dusty RV Tau stars.

**GK Car and GZ Nor.** GK Car (IRAS 11118-5726) and GZ Nor (IRAS 16278-5526) are two similar objects studied in detail by [Gezer et al. \(2019\)](#). From the ASAS-SN data, they determined the pulsation periods of 27.6 d for GK Car and 36.2 d for GZ Nor. The light curves folded on twice the period demonstrate alternating minima. The refractory elements are depleted in both stars which may indicate their binarity. The luminosities derived from the period-luminosity relation for the Type II Cepheids are significantly lower than the typical values for post-AGB stars. Based on the acquired results, [Gezer et al. \(2019\)](#) concluded that GK Car and GZ Nor are low-luminous, depleted RV Tau stars and have likely evolved off the RGB. GK Car and GZ Nor with the temperatures of 5500 and 4875 K, respectively, are cooler than IRAS 02143+5852.

## 8 CONCLUSIONS

The results of the photometric and spectroscopic observations of the post-AGB candidate IRAS 02143+5852 have been reported.

Based on our observational data we have found the star to vary in brightness with a period of 25 d and a *V*-band amplitude of 0.9 mag. The shape of light curves is typical for the Type II Cepheids. Its spectral properties, in particular the presence of the strong H $\alpha$  emission at certain phases of the pulsation cycle, are also characteristic for the Type II Cepheids.

IRAS 02143+5852 has a significant IR excess which is not usual for the W Vir stars, but is common among the RV Tau variables and is a determining feature of post-AGB objects. Modelling the SED in a wide wavelength range 0.44–160  $\mu$ m allowed us to derive the parameters of the dust circumstellar envelope. We show that it has a complicated structure and was produced by three episodes of mass loss (see Section 6).

Comparing IRAS 02143+5852 with similar objects leads to a conclusion that this star may be considered as a low-luminosity analogue of the dusty RV Tau stars. In order to clarify its evolutionary status it is highly necessary to obtain high-resolution spectra which can provide abundances and stellar parameters ( $T_{\text{eff}}$ ,  $\log g$ ).

Long-term high-resolution spectroscopic monitoring is also highly desirable to derive the radial velocity curve and possibly get evidence for the second component, as binarity is considered related to the existence of a powerful dust envelope. As was mentioned above, the presence of excess near-IR radiation is characteristic of post-AGB binary stars, and those of RV Tau type in particular ([Van Winckel 2017](#)).

In addition, it is necessary to continue the photometric monitoring to derive the so-called observed minus calculated (O-C) diagrams to be able to detect the possible light-time travel effect owing to the presence of a binary. Using the method proposed by [Hajdu et al. \(2015\)](#), [Groenewegen and Jurkovic \(2017\)](#) revealed 20 new possible binary systems among 335 Type II and anomalous Cepheids in the Small and Large Magellanic Clouds.

## ACKNOWLEDGMENTS

The work was carried out using the equipment purchased under the MSU Program of Development. We are indebted to the CMO staff observers and engineers who assisted in obtaining observations. We appreciate the comments of the referee, which led to considerable improvement in the paper. S.Yu. Shugarov (obtaining *BVRI*-photometry on the 0.6-m telescope at the Stará Lesná Observatory) acknowledges support from the Slovak Research and Development Agency (No. APVV-20-0148, APVV-15-0458) and the Slovak Academy of Sciences (grant VEGA No. 2/0030/21). The work of NPI (obtaining photometry with RC-600, analysis of the photometric and spectroscopic data) and AVD (spectrum processing) is supported by the RScF grant 23-12-00092. S.Zheltoukhov (obtaining NIR photometry with ASTRONIRCAM, dust model simulations) acknowledges the support of the Foundation for the Development of Theoretical Physics and Mathematics BASIS (project no. 21-2-10-35-1). The work of AMT (obtaining NIR photometry with ASTRONIRCAM, analysis of the results of SED modelling) is supported by the RScF grant 23-22-00182. We would like to thank the anonymous referee for the comments that helped to sharpen the text.

## DATA AVAILABILITY

The data underlying this study are available in the main body of the article and in online supplementary material.

## References

- Abt H.A., 1954, *ApJS*, 1, 63
- Alcock C., Allsman R.A., Alves D.R., Axelrod T.S., Becker A., Bennett D. P. et al., 1998, *AJ*, 115, 1921
- Aoki W., Matsuno T., Honda S., Parthasarathy M., Li H., Suda T., 2017, *PASJ*, 69, 21
- Bailer-Jones C.A.L., Rybizki J., Fouesneau M., Mantelet G., Andrae R., 2018, *ApJ*, 156, 58
- Bailer-Jones C.A.L., Rybizki J., Fouesneau M., Demleitner M., Andrae R., 2021, *AJ*, 161, 147
- Berdnikov L.N., Belinskii A.A., Shatskii N.I., Burlak M.A., Ikonnikova N.P., Mishin E.O., Cheryasov D.V., Zhuiko S.V., 2020, *Astron. Rep.*, 64, 310
- Berdnikov L. N., Yacob A. M., Pastukhova E. N., 2020, *Astronomy Letters*, 46, 630
- Bessell M. S. 1979, *PASP*, 91, 589
- Bopp B.W., 1984, *PASP*, 96, 432
- Cardelli J.A., Clayton G.C., Mathis J.S., 1989, *ApJ*, 345, 245
- Carpenter J.M., 2001, *AJ*, 121, 2851
- Cernicharo J., Marcelino N., Agundez M., Guelin M., 2015, *A&A*, 575, A91
- Chen X. Wang S., Deng L., de Grijs R. et al., 2020, *ApJS*, 249, 18
- Cooper H.D.B., Lumsden S.L., Oudmaijer R.D. et al., 2013, *MNRAS*, 430, 1125
- Cutri R. M., et al. 2013, *VizieR Online Data Catalog*, II/328
- Deeming T.J., 1975, *Ap&SS*, 36, 137
- De Ruyter S., Van Winckel H., Maas T., et al., 2006, *A&A*, 448, 641
- O'Donnell J.E., 1994, *ApJ*, 422, 158
- Dullemond C. P. , Juhasz A., Pohl A., Sereshti F., Shetty R., Peters T., Commercon B., Flock M., *Astrophysics Source Code Library*, ascl:1202.015 (2012)

- Egan M.P., Price S.D., Kraemer K.E., Mizuno D.R., Carey S.J., Wright C.O., Engelke C.W., Cohen M., Gugliotti M.G., 2003, VizieR Online Data Catalog: MSX6C Infrared Point Source Catalog. The Midcourse Space Experiment Point Source Catalog Version 2.3
- Fadeyev Yu. A., 2020, *Astronomy Letters*, 46, 734
- Fedoteva A.A., Tatarnikov A.M., Safonov B.S., Shenavrin V.I., Komissarova G.V., 2020, *Astronomy Letters*, 46, 38
- Flower P.J., 1977, *A&A*, 54, 31
- Flower P.J., 1996, *ApJ*, 469, 355
- Fujii T., Nakada Y., Parthasarathy M., 2002, *A&A*, 385, 884
- Gaia Collaboration; Brown A. G. A., Vallenari A., Prusti T. et al., 2018, *A&A*, 616, 10
- Gaia Collaboration, 2022, VizieR On-line Data Catalog: I/355
- García-Lario P., Manchado A., Pottasch S. R., Suso, J., Olling R., 1990, *A&AS*, 82, 497
- Gezer I., Van Winckel H., Manick R., Kamath D., 2019, *MNRAS*, 488, 4033
- Gerasimovič B.P., 1929, *Harvard College Observatory Circular*, 341, 1
- Gingold R.A., 1974, *ApJ*, 193, 177
- Gingold R.A., 1976, *ApJ*, 204, 116
- Gingold R.A., 1985, *Memorie della Societa Astronomica Italiana*, 56, 169
- Gledhill T.M., 2005, *MNRAS*, 356, 883
- Green G. M., Schlafly E., Zucker C., Speagle J.S., Finkbeiner D., 2019, *ApJ*, 887, 93
- Groenewegen M.A.T., Jurkovic M.I., 2017, *A&A*, 604, A29
- Hajdu G., Catelan M., Jurcsik J., Dekany I., Drake A. J., Marquette J.-B., 2015, *MNRAS*, 49, L113
- Harris H.C., 1985, *AJ*, 90, 756
- Harris H.C., Wallerstein G., 1984, *AJ*, 89, 379
- Helou G., Walker D.W., 1988, *Infrared astronomical satellite (IRAS) catalogs and atlases. Volume 7*, p.1-265
- Hofner S., 2008, *A&A*, 491, L1
- Inno L., Matsunaga N., Romaniello M. et al., 2015, *A&A*, 576, A30
- Jarrett T.H., Cohen M., Masci F., et al., 2011, *ApJ*, 735, 112
- Jayasinghe T., Stanek K. Z., Kochanek C. S., et al., 2019, *MNRAS*, 486, 1907
- Jura M., Turner J., Balm S.P., 1997, *ApJ*, 474, 741
- Kelly D.M., Hrivnak B.J., 2005, *ApJ*, 629, 1040
- Kiss A.A., DEREKAS A., Szabó Gy.M., Bedding T.R., Szabados L., 2007, *MNRAS*, 375, 1338
- Kochanek C.S., Shappee B.J., Stanek K.Z., Holohan T.W.-S., Thompson, Todd A. et al., 2017, *PASP*, 129:104502
- Koornneef J., 1983, *A&A*, 128, 84
- Kovtuykh V.V., Wallerstein G., Andrievsky S.M., Gillet D., 2011, *A&A*, 526, A116
- Lafler J., Kinman T.D., 1965, *ApJS*, 11, 216L
- Landolt A.U., 2013, *AJ*, 146, 131
- Leggett S.K., Currie M.J., Varricatt W.P., 2006, *MNRAS*, 273, 781
- Maas T., Giridhar S., Lambert D. L., 2007, *ApJ*, 666, 378
- Manchado A., Pottasch S.R., García-Lario P., Esteban C., Mampaso A., 1989, *A&A*, 214, 139
- Manick R., Van Winckel H., Kamath D., Hillen M., Escorza A., 2017, *A&A*, 597, A129
- Mantegazza L., 1991, *A&AS*, 88, 255
- Mattsson L., Wahlin R., Hofner S., 2010, *A&A*, 509, A14
- Mauron N., Huggins P. J., 2000, *A&A*, 359, 707
- Meixner M., Ueta T., Dayal A. et al., 1999, *ApJS*, 122, 221
- Miller Bertolami M.M., 2016, *A&A*, 588, A25
- Molina R.E., 2018, *Rev. Mex. Astron. Astrofis.*, 54, 397
- Murakami H., Baba H., Barthel P., 2007, *PASJ*, 59, 369
- Nadjip A.E., Tatarnikov A.M., Toomey D.W., Shatsky N.I., Cherepashchuk A.M., Lamzin S. A., Belinski A. A., 2017, *Astrophysical Bulletin*, 72, 349
- Norris B.R.M., Tuthill P.G., Ireland M.J., Lacour S., Zijlstra A.A., Lykou F., Evans T.M., Stewart P., Bedding T.R., 2012, *Nature*, 484, 220
- Ohnaka K., Weigelt G., Hofmann K.H., 2017, *A&A*, 597, A20
- Omont A., Loup C., Forveille T., et al., 1993, *A&A*, 267, 515
- Pickles A.J., 1998, *PASP*, 110, 863
- Plachy E., Kovács G.B. and Forgács-Dajka E., 2018, in *Revival of the Classical Pulsators: from Galactic Structure to Stellar Interior Diagnostics*, Proceedings of the Polish Astronomical Society, vol. 6., p. 310
- Pollard K. R., Cottrell P. L., Kilmartin P. M., Gilmore A. C., 1996, *MNRAS*, 279, 949
- Pollard K. R., Cottrell P. L., Lawson W. A., Albrow M. D., Tobin W., 1997, *MNRAS*, 286, 1
- Potarin S.A., Belinskii A.A., Dodin A.V. et al., 2020, *Astron. Lett.*, 46, 837
- Ramstedt S., Schoier F.L., Olofsson H., 2009, *A&A*, 499, 515
- Rudy, R. J., Subasavage, J. P., Mauerhan, J. C. et al., 2021, *AJ*, 161, 291
- Saario J.L.O., Groenewegen M.A.T., Van Winckel H., 2018, *Proceedings of the Polish Astronomical Society*, vol. 6, 314
- Samus N.N., Kazarovets E.V., Durlevich O.V., Kireeva N.N., Pastukhova E.N., 2017, *Astron. Rep.*, 61, 80
- Schmidt E.G., 2015, *ApJ*, 813, 29
- Schmidt E.G., Johnston D., Langan S., Lee K.M., 2004a, *AJ*, 128, 1748
- Schmidt E.G., Johnston D., Lee K.M., Langan S., 2004b, *AJ*, 128, 2988
- Shappee B.J., Prieto J.L., Grupe D., Kochanek C.S., Stanek K. Z., De Rosa G., 2014, *ApJ*, 788, 48
- Shenton M., Evans A., Williams P.M., 1995, *MNRAS*, 273, 906
- Simons D.A. and Tokunaga A., 2002, *PASP*, 114, 169
- Sivarani T., Parthasarathy M., 2004, in Penny A., eds., *Proc. IAU Symp. 202, Planetary Systems in the Universe Proceedings*. Cambridge Univ. Press, Cambridge, p. 371
- Smolec R., Soszyński I., Moskalik P., Udalski A., Szymański M.K., Kubiak M., Pietrzyński G., Wyrzykowski Ł., Ulaczyk K., Poleski R., Kozłowski S., Pietrukowicz P., 2012, *MNRAS*, 419, 2407
- Straizys V., 1982, *Metal-Deficient Stars*. Mokslas, Vilnius
- Straizys V., 1992, *Multicolor stellar photometry*. Pachart Publishing House, Tucson
- Suárez O., García-Lario P., Manchado A., Manteiga M., Ulla A., Pottasch S.R., 2006, *A&A*, 458, 173
- Suárez O., Gómez J.F., Morata O., 2007, *A&A*, 467, 1085
- Suh K.W., 2000, *MNRAS*, 315, 740
- Szabó R., Kolláth Z., Molnár L. et al., 2010, *MNRAS*, 409, 1244
- Tatarnikov A.M., Zheltoukhov S.G., Shatsky N.I., Burlak M.A., Maslennikova N.A., Vakhonin A.A., 2023, *Astrophys. Bull.*, 78, 259
- Templeton M.R., Henden A.A., 2007, *AJ*, 134, 1999
- Tokunaga A.T., Vacca W.D., 2005, *PASP*, 117, 421
- Ueta T., Meixner M., Moser D.E., Pyzowski L.A., Davis J.S., 2003, *AJ*, 125, 2227
- Wallerstein G., 1959, *ApJ*, 130, 560
- Van Winckel H., 2017, in Liu X., Stanghellini L., Karakas A., eds., *Proc. IAU Symp. 323, Planetary Nebulae: Multi-Wavelength Probes of Stellar and Galactic Evolution*. Cambridge Univ. Press, Cambridge, p. 231
- Van Winckel H., Hrivnak B.J., Gorlova N., Gielen C., Lu W., 2012, *A&A*, 542, A53
- Whitney C., 1956, *Annales d'Astrophysique*, 19, 142

**APPENDIX A:  $UBVR_C I_C$ -OBSERVATIONS OF IRAS 02143+5852 IN 2018-2021**Table A1:  $UBVR_C I_C$ -observations of IRAS 02143+5852 in 2018-2021

JD	$U$	$B$	$V$	$R_C$	$I_C$	Telescope
2458133.219	15.830	15.389	14.160	13.410	12.609	SI600
2458134.254	15.605	15.166	14.004	13.272	12.494	SI600
2458165.308	15.144	14.762	13.586	12.865	12.065	SI600
2458169.342	15.503	14.923	13.645	12.884	12.050	SI600
2458175.249	16.143	15.331	13.987	13.157	12.294	SI600
2458182.360	16.160	15.624	14.350	13.548	12.729	SI600
2458186.334	15.146	14.740	13.606	12.925	12.194	SI600
2458187.324	15.040	14.646	13.527	12.840	12.103	SI600
2458188.278	15.121	14.658	13.534	12.842	12.072	SI600
2458215.320	15.306	14.885	13.665	12.907	12.129	SI600
2458218.304	15.459	14.927	13.656	12.872	12.069	SI600
2458220.304	15.545	14.998	13.693	12.905	12.005	SI600
2458360.539	15.282	14.932	13.783	13.103	12.338	SI600
2458364.479	15.188	14.776	13.605	12.896	12.117	SI600
2458378.449	16.443	15.706	14.307	13.459	12.590	SI600
2458379.442	16.531	15.781	14.387	13.537	12.664	SI600
2458380.436	16.519	15.811	14.430	13.583	12.722	SI600
2458381.427	16.523	15.783	14.438	13.603	12.750	SI600
2458391.461	15.354	14.848	13.649	12.906	12.096	SI600
2458396.434	15.724	15.067	13.779	12.999	12.157	SI600
2458397.479	15.782	15.159	13.840	13.051	12.209	SI600
2458406.496	16.038	15.519	14.255	13.480	12.651	SI600
2458407.385	15.949	15.462	14.244	13.474	12.662	SI600
2458453.573	16.132	15.489	14.174	13.355	12.504	SI600
2458471.329	15.773	15.105	13.825	13.038	12.193	SI600
2458530.337	16.575	15.794	14.424	13.560	12.707	SI600
2458685.524	15.402	14.969	13.836	13.145	12.390	SI600
2458686.460	15.194	14.769	13.675	13.012	12.266	SI600
2458699.526	16.124	15.410	14.063	13.235	12.418	RC600
2458703.536	16.296	15.723	14.357	13.529	12.669	RC600
2458711.514	15.272	14.675	13.626	12.948	12.208	RC600
2458716.494	15.527	15.004	13.736	12.980	12.181	RC600
2458719.401	15.793	15.065	13.785	12.991	12.204	SI600
2458724.443	16.132	15.422	14.052	13.227	12.405	RC600
2458725.522	16.255	15.526	14.138	13.304	12.450	RC600
2458726.500	16.358	15.601	14.228	13.380	12.551	RC600
2458726.583	16.359	15.626	14.241	13.418	12.563	SI600
2458727.388	16.359	15.678	14.290	13.438	12.619	RC600
2458728.467	16.395	15.738	14.360	13.518	12.676	RC600
2458729.499	16.474	15.798	14.433	13.607	12.767	RC600
2458730.514	16.441	15.831	14.465	13.663	12.780	RC600
2458732.571	16.281	15.718	14.430	13.639	12.836	RC600
2458735.502	15.293	14.734	13.682	13.001	12.268	RC600
2458738.481	15.264	14.702	13.607	12.878	12.140	RC600
2458739.548	15.379	14.791	13.653	12.912	12.146	RC600
2458740.534	15.491	14.868	13.686	12.927	12.147	RC600
2458741.535	15.527	14.904	13.701	12.939	12.133	RC600
2458742.541	15.568	14.951	13.713	12.948	12.135	RC600
2458744.517	15.736	15.035	13.767	12.982	12.174	RC600
2458745.520	15.756	15.085	13.808	13.018	12.197	RC600
2458746.509	15.827	15.150	13.870	13.055	12.235	RC600
2458749.495	16.055	15.386	14.048	13.209	12.388	RC600
2458750.554	16.133	15.474	14.132	13.292	12.466	RC600
2458758.595	15.507	15.113	13.996	13.303	12.548	SI600
2458761.395	15.167	14.644	13.601	12.915	12.185	RC600
2458764.428	15.478	14.915	13.735	12.988	12.197	RC600



continued TableA1

JD	<i>U</i>	<i>B</i>	<i>V</i>	<i>R<sub>C</sub></i>	<i>I<sub>C</sub></i>	Telescope
2458766.398	15.646	14.982	13.745	12.975	12.176	RC600
2458767.306	15.710	15.012	13.757	12.975	12.171	RC600
2458769.509	15.795	15.099	13.798	13.009	12.200	RC600
2458770.428	15.883	15.138	13.825	13.034	12.219	RC600
2458770.593	15.875	15.160	13.869	13.041	12.231	SI600
2458771.402	16.003	15.194	13.878	13.045	12.248	RC600
2458771.566	16.210	15.226	13.892	13.105	12.269	SI600
2458772.561	16.005	15.302	13.973	13.169	12.332	SI600
2458773.393	16.104	15.401	14.028	13.210	12.383	RC600
2458774.296	16.268	15.526	14.122	13.281	12.451	RC600
2458774.420	16.270	15.557	14.165	13.320	12.470	SI600
2458775.354	16.293	15.647	14.228	13.387	12.552	RC600
2458776.377	16.435	15.728	14.313	13.466	12.621	RC600
2458776.558	16.474	15.730	14.354	13.505	12.652	SI600
2458777.411	16.546	15.806	14.387	13.549	12.710	RC600
2458778.345	16.567	15.872	14.461	13.615	12.768	RC600
2458779.396	16.558	15.907	14.519	13.679	12.843	RC600
2458780.344	16.535	15.906	14.534	13.710	12.883	RC600
2458781.348	16.385	15.761	14.491	13.676	12.855	RC600
2458782.436	16.000	15.468	14.253	13.485	12.682	RC600
2458782.494	15.931	15.464	14.240	13.479	12.678	SI600
2458783.286	15.609	15.111	13.981	13.260	12.493	RC600
2458784.362	15.198	14.775	13.665	12.994	12.253	SI600
2458784.388	15.284	14.731	13.677	12.986	12.250	RC600
2458785.476	15.159	14.603	13.559	12.883	12.140	RC600
2458786.320	15.151	14.620	13.556	12.860	12.129	RC600
2458790.349	15.469	14.873	13.680	12.912	12.124	RC600
2458791.393	15.536	14.904	13.691	12.917	12.122	RC600
2458792.447	15.643	14.949	13.701	12.934	12.133	RC600
2458794.348	15.785	15.053	13.782	12.987	12.178	RC600
2458795.505	15.864	15.140	13.841	13.040	12.221	RC600
2458796.312	15.962	15.203	13.889	13.077	12.251	RC600
2458797.398	16.026	15.297	13.964	13.145	12.320	RC600
2458798.217	16.094	15.383	14.033	13.206	12.373	RC600
2458799.312	16.225	15.516	14.140	13.288	12.467	RC600
2458800.346	16.197	15.609	14.222	13.388	12.550	RC600
2458802.254	16.413	15.748	14.386	13.548	12.701	RC600
2458803.358	16.436	15.782	14.452	13.613	12.786	RC600
2458804.310	16.376	15.775	14.470	13.642	12.825	RC600
2458805.297	16.288	15.682	14.437	13.639	12.827	RC600
2458806.324	15.910	15.430	14.282	13.523	12.741	RC600
2458807.351	15.603	15.086	14.015	13.297	12.546	RC600
2458808.256	15.320	14.813	13.777	13.085	12.350	RC600
2458810.232	15.111	14.582	13.539	12.856	12.124	RC600
2458811.494	15.167	14.665	13.575	12.872	12.121	RC600
2458812.343	15.277	14.734	13.604	12.884	12.114	RC600
2458813.392	15.409	14.826	13.649	12.900	12.114	RC600
2458816.480	15.602	14.979	13.714	12.931	12.123	RC600
2458818.382	15.730	15.039	13.760	12.968	12.151	RC600
2458820.397	15.849	15.148	13.840	13.025	12.205	RC600
2458822.393	16.053	15.322	13.963	13.142	12.314	RC600
2458823.373	16.195	15.420	14.043	13.208	12.379	RC600
2458824.420	16.228	15.520	14.129	13.287	12.460	RC600
2458825.381	16.308	15.601	14.204	13.373	12.532	RC600
2458826.381	16.370	15.678	14.282	13.454	12.612	RC600
2458827.377	16.438	15.730	14.362	13.520	12.689	RC600
2458828.370	16.410	15.761	14.401	13.572	12.738	RC600
2458829.406	16.552	15.749	14.405	13.597	12.771	RC600
2458830.386	16.174	15.632	14.352	13.545	12.741	RC600
2458833.363	15.357	14.841	13.764	13.063	12.314	RC600

continued TableA1

JD	<i>U</i>	<i>B</i>	<i>V</i>	<i>R<sub>C</sub></i>	<i>I<sub>C</sub></i>	Telescope
2458834.302	15.224	14.695	13.640	12.951	12.204	RC600
2458835.306	15.182	14.663	13.598	12.901	12.160	RC600
2458836.289	15.209	14.699	13.615	12.909	12.156	RC600
2458837.263	15.308	14.750	13.652	12.924	12.150	RC600
2458838.277	15.342	14.811	13.666	12.926	12.151	RC600
2458840.352	15.474	14.892	13.676	12.918	12.131	RC600
2458841.376	15.543	14.932	13.695	12.929	12.134	RC600
2458843.314	15.645	15.012	13.745	12.948	12.154	RC600
2458844.294	15.702	15.046	13.780	12.991	12.182	RC600
2458846.340	15.849	15.185	13.877	13.075	12.249	RC600
2458847.403	15.936	15.275	13.950	13.137	12.317	RC600
2458847.475	15.909	15.299	13.976	13.179	12.325	SI600
2458848.277	15.984	15.344	14.013	13.193	12.371	RC600
2458849.240	16.008	15.406	14.083	13.259	12.431	RC600
2458851.271	16.143	15.518	14.203	13.396	12.571	RC600
2458852.236	16.146	15.541	14.252	13.438	12.631	RC600
2458853.272	16.101	15.550	14.301	13.504	12.696	RC600
2458854.436	16.064	15.550	14.319	13.523	12.723	RC600
2458855.224	15.988	15.506	14.292	13.513	12.721	RC600
2458855.263	15.930	15.493	14.252	13.510	12.711	SI600
2458856.339	15.747	15.278	14.095	13.384	12.590	SI600
2458857.266	15.582	15.026	13.958	13.225	12.477	RC600
2458859.215	15.213	14.650	13.599	12.915	12.178	SI600
2458859.262	15.115	14.682	13.562	12.899	12.161	SI600
2458862.221	15.377	14.817	13.672	12.936	12.160	RC600
2458863.217	15.472	14.876	13.698	12.947	12.157	RC600
2458863.299	15.405	14.907	13.683	12.946	12.136	SI600
2458865.229	15.571	14.940	13.700	12.931	12.131	RC600
2458866.238	15.649	14.972	13.709	12.925	12.133	SI600
2458867.199	15.698	14.999	13.725	12.949	12.135	RC600
2458867.241	15.750	15.032	13.743	12.972	12.151	SI600
2458868.227	15.737	15.033	13.751	12.977	12.152	RC600
2458869.252	15.806	15.084	13.787	12.988	12.179	RC600
2458870.176	15.838	15.146	13.827	13.024	12.210	RC600
2458871.214	15.934	15.226	13.909	13.089	12.265	RC600
2458873.199	16.155	15.497	14.102	13.253	12.418	RC600
2458874.360	16.239	15.610	14.195	13.346	12.506	RC600
2458876.325	16.371	15.767	14.329	13.482	12.641	RC600
2458877.190	16.394	15.794	14.389	13.543	12.713	RC600
2458878.193	16.411	15.837	14.435	13.609	12.775	RC600
2458881.211	15.890	15.387	14.197	13.433	12.646	RC600
2458883.307	15.131	14.645	13.607	12.929	12.190	RC600
2458884.203	15.030	14.522	13.496	12.831	12.093	RC600
2458887.165	15.276	14.694	13.563	12.847	12.074	RC600
2458889.309	15.439	14.814	13.628	12.858	12.073	RC600
2458890.186	15.483	14.855	13.640	12.872	12.074	RC600
2458891.189	15.541	14.897	13.663	12.889	12.078	RC600
2458892.224	15.590	14.959	13.700	12.924	12.111	RC600
2458894.207	15.743	15.082	13.785	12.978	12.163	RC600
2458895.287	15.808	15.179	13.839	13.042	12.224	RC600
2458896.253	15.934	15.264	13.909	13.096	12.261	RC600
2458897.266	15.981	15.357	13.981	13.163	12.321	RC600
2458898.211	16.065	15.436	14.054	13.225	12.402	RC600
2458899.251	16.087	15.511	14.115	13.293	12.471	RC600
2458900.361	16.142	15.585	14.203	13.377	12.562	RC600
2458901.328	16.122	15.640	14.272	13.448	12.627	RC600
2458902.300	16.244	15.657	14.357	13.479	12.678	RC600
2458903.305	16.173	15.652	14.349	13.541	12.714	RC600
2458905.216	15.892	15.407	14.248	13.479	12.690	RC600
2458906.229	15.490	15.065	13.979	13.256	12.492	RC600

continued TableA1

JD	<i>U</i>	<i>B</i>	<i>V</i>	<i>R<sub>C</sub></i>	<i>I<sub>C</sub></i>	Telescope
2458908.237	14.979	14.508	13.496	12.836	12.122	RC600
2458909.203	15.020	14.514	13.483	12.813	12.083	RC600
2458911.223	15.244	14.720	13.597	12.870	12.091	RC600
2458912.208	15.338	14.801	13.628	12.877	12.088	RC600
2458913.210	15.408	14.844	13.645	12.882	12.082	RC600
2458914.212	15.474	14.887	13.657	12.881	12.075	RC600
2458917.194	15.616	14.986	13.702	12.906	12.093	RC600
2458918.232	15.666	15.028	13.738	12.935	12.126	RC600
2458919.209	15.793	15.099	13.779	12.979	12.159	RC600
2458922.246	16.006	15.430	14.032	13.187	12.358	RC600
2459050.529	16.166	15.581	14.262	13.426	12.606	RC600
2459051.519	16.217	15.642	14.313	13.492	12.666	RC600
2459055.528	15.378	14.930	13.872	13.147	12.421	RC600
2459061.510	15.257	14.767	13.603	12.853	12.053	RC600
2459067.498	15.725	15.028	13.725	12.926	12.107	RC600
2459068.456	15.782	15.094	13.780	12.971	12.143	RC600
2459070.469	15.995	15.301	13.927	13.092	12.256	RC600
2459079.550	15.810	15.283	14.102	13.338	12.551	RC600
2459081.448	15.243	14.725	13.660	12.953	12.220	RC600
2459082.472	15.110	14.570	13.536	12.838	12.106	RC600
2459084.503	15.130	14.605	13.525	12.820	12.064	RC600
2459087.396	15.321	14.762	13.585	12.833	12.036	RC600
2459088.327	15.383	14.818	13.609	12.841	12.035	RC600
2459090.527	15.554	14.903	13.653	12.871	12.058	RC600
2459091.545	15.617	14.972	13.693	12.899	12.082	RC600
2459092.499	15.719	15.039	13.736	12.936	12.115	RC600
2459093.450	15.784	15.108	13.792	12.982	12.157	RC600
2459094.488	15.874	15.196	13.855	13.046	12.208	RC600
2459095.447	15.918	15.275	13.923	13.104	12.265	RC600
2459097.488	16.030	15.420	14.067	13.240	12.404	RC600
2459099.437	16.074	15.499	14.179	13.390	12.544	RC600
2459103.417	15.780	15.312	14.159	13.390	12.610	RC600
2459104.492	15.568	15.093	13.986	13.251	12.479	RC600
2459106.506	15.168	14.651	13.603	12.910	12.170	RC600
2459108.568	15.151	14.601	13.528	12.818	12.070	RC600
2459109.364	15.202	14.684	13.566	12.833	12.079	RC600
2459110.325	15.350	14.766	13.605	12.860	12.094	RC600
2459112.515	15.509	14.883	13.650	12.879	12.080	RC600
2459113.278	15.584	14.932	13.675	12.879	12.084	RC600
2459114.517	15.605	14.932	13.675	12.892	12.086	RC600
2459115.260	15.673	14.971	13.685	12.901	12.097	RC600
2459117.464	15.821	15.062	13.752	12.957	12.153	RC600
2459118.287	15.813	15.110	13.798	12.998	12.181	RC600
2459119.312	15.929	15.208	13.869	13.052	12.247	RC600
2459120.381	16.086	15.323	13.953	13.136	12.302	RC600
2459121.407	16.104	15.455	14.062	13.211	12.382	RC600
2459126.457	16.296	15.711	14.382	13.532	12.721	RC600
2459129.448	15.919	15.339	14.154	13.374	12.589	RC600
2459130.487	15.519	14.972	13.858	13.132	12.372	RC600
2459131.303	15.210	14.693	13.642	12.950	12.217	RC600
2459132.374	15.070	14.529	13.483	12.813	12.090	RC600
2459136.461	15.262	14.696	13.538	12.793	12.018	RC600
2459138.490	15.396	14.807	13.594	12.819	12.020	RC600
2459140.460	15.557	14.904	13.645	12.864	12.048	RC600
2459145.560	15.935	15.272	13.930	13.114	12.274	RC600
2459146.445	15.992	15.334	13.994	13.178	12.337	RC600
2459149.469	16.157	15.543	14.223	13.391	12.578	RC600
2459150.524	16.123	15.558	14.262	13.441	12.621	RC600
2459152.451	16.043	15.440	14.233	13.450	12.664	RC600
2459153.440	15.750	15.263	14.111	13.387	12.592	RC600

continued Table A1

JD	<i>U</i>	<i>B</i>	<i>V</i>	<i>R<sub>C</sub></i>	<i>I<sub>C</sub></i>	Telescope
2459158.447	15.204	14.652	13.564	12.852	12.099	RC600
2459162.502	15.467	14.859	13.631	12.865	12.071	RC600
2459163.436	15.518	14.885	13.646	12.864	12.075	RC600
2459164.382	15.527	14.918	13.661	12.879	12.076	RC600
2459165.385	15.614	14.947	13.677	12.893	12.088	RC600
2459166.307	15.699	14.984	13.709	12.921	12.106	RC600
2459167.389	15.752	15.042	13.748	12.953	12.141	RC600
2459175.480	16.394	15.646	14.273	13.440	12.612	RC600
2459177.416	16.313	15.684	14.343	13.517	12.711	RC600
2459181.399	15.353	14.793	13.703	13.000	12.266	RC600
2459182.359	15.200	14.624	13.566	12.875	12.135	RC600
2459183.445	15.147	14.590	13.525	12.833	12.077	RC600
2459196.309	15.957	15.344	13.987	13.172	12.343	RC600
2459251.359	16.019	15.601	14.344	13.560	12.766	RC600

**APPENDIX B: *JHK*-OBSERVATIONS OF IRAS 02143+5852 IN 2017–2021**Table B1: *JHK*-observations of IRAS 02143+5852 in 2017–2021.

JD	<i>J</i> (MKO)	<i>H</i> (MKO)	<i>K</i> (MKO)	<i>J</i> (2MASS)	<i>H</i> (2MASS)	<i>K</i> (2MASS)
2458064.331	10.644	9.620	8.482	10.809	9.578	8.571
2458089.324	10.614	9.534	8.366	10.785	9.491	8.457
2458099.152	10.753	9.759	8.657	10.912	9.719	8.743
2458144.318	10.502	9.494	8.366	10.665	9.453	8.454
2458147.243	10.608	9.632	8.521	10.767	9.592	8.608
2458151.360	10.831	9.839	8.731	10.991	9.799	8.818
2458153.394	10.974	9.976	8.873	11.134	9.936	8.959
2458156.259	11.157	10.129	8.970	11.324	10.086	9.060
2458157.168	11.177	10.121	8.947	11.347	10.077	9.038
2458158.187	11.121	10.048	8.852	11.294	10.003	8.945
2458166.282	10.553	9.535	8.388	10.718	9.493	8.477
2458172.339	10.629	9.663	8.533	10.788	9.622	8.621
2458180.208	11.193	10.259	9.224	11.343	10.222	9.305
2458480.497	11.172	10.207	9.142	11.326	10.169	9.226
2458481.238	11.214	10.250	9.168	11.370	10.211	9.253
2458482.356	11.278	10.307	9.227	11.434	10.268	9.312
2458483.283	11.299	10.308	9.199	11.459	10.268	9.286
2458484.294	11.279	10.273	9.134	11.442	10.231	9.223
2458486.385	11.035	9.919	8.665	11.216	9.872	8.762
2458487.340	10.844	9.687	8.380	11.032	9.637	8.481
2458489.326	10.645	9.492	8.207	10.831	9.443	8.306
2458493.380	10.657	9.597	8.421	10.827	9.553	8.512
2458511.491	10.988	9.849	8.550	11.174	9.799	8.650
2458513.377	10.733	9.573	8.314	10.918	9.525	8.411
2458520.406	10.666	9.648	8.512	10.830	9.606	8.601
2458862.309	10.652	9.598	8.436	10.821	9.555	8.527
2458866.295	10.611	9.640	8.524	10.770	9.599	8.611
2458867.256	10.638	9.661	8.559	10.796	9.621	8.645
2458868.292	10.640	9.694	8.599	10.795	9.654	8.685
2458869.381	10.685	9.739	8.650	10.840	9.700	8.735
2458870.398	10.732	9.789	8.718	10.885	9.751	8.802
2458871.173	10.784	9.828	8.771	10.937	9.790	8.854
2458877.203	11.234	10.286	9.274	11.383	10.250	9.354
2458879.174	11.377	10.385	9.334	11.532	10.348	9.417
2458884.287	10.605	9.494	8.240	10.785	9.447	8.337
2458908.162	10.639	9.490	8.211	10.824	9.441	8.310

continued TableB1

JD	<i>J</i> (MKO)	<i>H</i> (MKO)	<i>K</i> (MKO)	<i>J</i> (2MASS)	<i>H</i> (2MASS)	<i>K</i> (2MASS)
2458911.153	10.609	9.585	8.436	10.774	9.543	8.526
2458912.175	10.598	9.596	8.481	10.759	9.555	8.568
2458914.159	10.572	9.587	8.494	10.730	9.547	8.580
2458916.191	10.579	9.612	8.513	10.736	9.572	8.599
2458918.161	10.621	9.673	8.593	10.775	9.634	8.678
2458919.171	10.663	9.710	8.648	10.816	9.672	8.731
2458920.193	10.724	9.778	8.724	10.876	9.740	8.807
2459084.503	10.559	9.463	8.251	10.735	9.418	8.345
2459091.541	10.579	9.601	8.483	10.738	9.560	8.570
2459095.448	10.776	9.813	8.735	10.931	9.774	8.820
2459141.444	10.568	9.579	8.449	10.730	9.538	8.537
2459149.469	11.058	10.072	8.976	11.216	10.032	9.062
2459153.340	11.101	10.030	8.797	11.276	9.984	8.893
2459155.362	10.843	9.708	8.411	11.028	9.659	8.511
2459161.566	10.571	9.523	8.347	10.740	9.480	8.438
2459165.399	10.577	9.573	8.432	10.744	9.529	8.521
2459171.457	10.851	9.890	8.805	11.007	9.851	8.890
2459175.491	11.134	10.193	9.116	11.288	10.154	9.200
2459194.435	10.714	9.750	8.629	10.872	9.709	8.716
2459195.356	10.775	9.802	8.705	10.933	9.762	8.791
2459196.297	10.838	9.871	8.781	10.994	9.831	8.866
2459199.299	11.070	10.092	8.995	11.228	10.053	9.081
2459201.303	11.186	10.207	9.096	11.345	10.167	9.183
2459206.213	10.697	9.529	8.221	10.887	9.479	8.322
2459208.145	10.614	9.479	8.209	10.798	9.431	8.307
2459209.141	10.611	9.522	8.301	10.787	9.476	8.396
2459211.209	10.599	9.548	8.371	10.769	9.504	8.463
2459220.222	10.846	9.888	8.808	11.001	9.849	8.892
2459224.299	11.169	10.237	9.184	11.320	10.200	9.267
2459239.410	10.583	9.585	8.425	10.748	9.542	8.515
2459245.151	10.848	9.866	8.761	11.007	9.825	8.848
2459246.260	10.929	9.956	8.865	11.086	9.917	8.950
2459255.160	10.814	9.659	8.348	11.003	9.608	8.449
2459257.214	10.636	9.515	8.248	10.818	9.467	8.346
2459258.143	10.623	9.530	8.292	10.801	9.483	8.388
2459264.350	10.603	9.597	8.441	10.768	9.554	8.531